J. Fluid Mech. (2019), *vol.* 877, *pp.* 239–281. © Cambridge University Press 2019
doi:10.1017/jfm.2019.559

Large-scale motions in a plane wall jet

Ebenezer P. Gnanamanickam[1],†, Shibani Bhatt[1], Sravan Artham[1] and Zheng Zhang[1]

[1]Department of Aerospace Engineering, Embry-Riddle Aeronautical University, FL 32114, USA

(Received 17 August 2018; revised 5 July 2019; accepted 7 July 2019;
first published online 19 August 2019)

The plane wall jet (PWJ) is a wall-bounded flow in which a wall shear layer develops in the presence of extremely energetic flow structures of the outer free-shear layer. The structure of a PWJ, developing in still air, was studied with the focus on the large scales in the flow. Wall-normal hot-wire anemometry (HWA) measurements along with double-frame particle image velocimetry (PIV) measurements (wall-normal–streamwise plane) were carried out at streamwise distances up to $162b$, where b is the slot width of the PWJ exit. The nominal PWJ Reynolds number based on exit parameters was $Re_j \approx 5940$. Comparisons with a zero-pressure-gradient boundary layer (ZPGBL) at nominally matched friction Reynolds number Re_τ were also carried out as appropriate, to highlight key features of the PWJ structure. Consistent with previous work, the PWJ showed a dependence of the peak turbulent stresses on the jet exit Reynolds number. The turbulent production showed a peak corresponding to the near-wall cycle similar to the peak seen in the ZPGBL. However, another turbulent production peak was observed in the outer free-shear layer that was an order of magnitude larger than the inner one. Along with the change in sign of the viscous and Reynolds shear stresses, the PWJ was shown to have a region of very low turbulent production between these two peaks. The dissipation rate increased over the PWJ layer with a peak also in the outer region. Visualizations of the flow and two-point correlations reveal that the most energetic large-scale structures within a PWJ are vortical motions in the wall-normal–streamwise plane similar to those structures seen in free-shear layers. These structures are referred to as J (for jet) type structures. In addition two-point correlations reveal the existence of large-scale structures in the wall region which have a signature similar to those structures seen in canonical boundary layers. These structures are referred to as W (for wall) type structures. Instantaneous PIV realizations and flow visualizations reveal that these W type large-scale features are consistent with the paradigm of hairpin vortex packets in the wall region. The J type structures were seen to intrude well into the wall region while the W type structures were also seen to extend into the outer shear layer. Further, these large-scale structures were shown to modulate the amplitude of the finer scales of the flow.

Key words: boundary layer structure, turbulent boundary layers

† Email address for correspondence: gnanamae@erau.edu

https://doi.org/10.1017/jfm.2019.559 Published online by Cambridge University Press

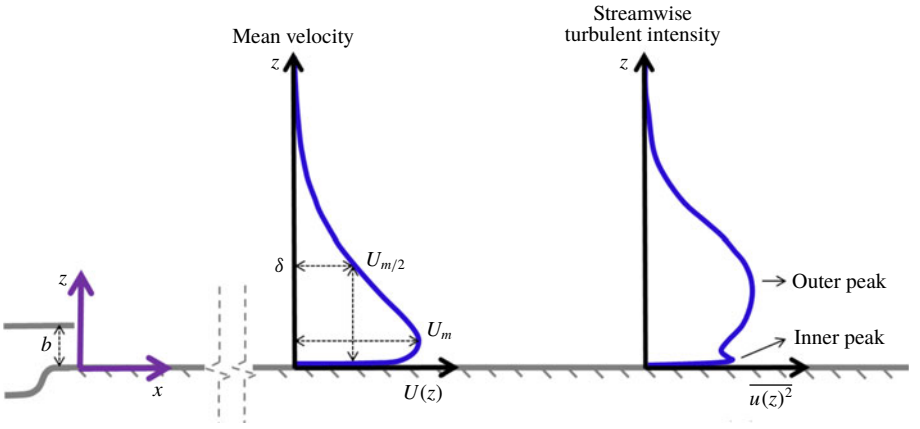


FIGURE 1. (Colour online) Schematic highlighting the salient features of a plane wall jet. A typical self-similar velocity profile $U(z)$ is shown along with a typical streamwise turbulent intensity profile $\overline{u(z)^2}$. The streamwise and wall-normal ordinates are x and z respectively. The jet exit width is b while the outer length scale is δ and the outer velocity scale is U_m, as highlighted. The turbulence peaks associated with the inner boundary layer and the outer jet portion of the PWJ are also highlighted.

1. Introduction

The turbulent plane wall jet (PWJ) is a flow field encountered in several engineering applications. For example, PWJ type flows are encountered in the boundary-layer development of multi-element airfoils, in the film cooling of turbine blades and combustion chambers (Launder & Rodi 1983; Wygnanski, Katz & Horev 1992), in drying/demisting applications (Dejoan & Leschziner 2005) as well as when a rotorcraft is operating in ground effect (Rauleder & Leishman 2014). The present work focuses on the PWJ developing in still air. A schematic highlighting its various salient features including a typical self-similar streamwise velocity profile $U(z)$ and a streamwise turbulence intensity profile $\overline{u(z)^2}$ is shown in figure 1. Here, z is the wall-normal direction.

Early investigations of the PWJ have been reviewed in some detail by Launder & Rodi (1981, 1983). The focus of most of these early studies and a vast majority of the work since, has been on reporting turbulence statistics. With the exception of the works cited in the following discussion, the structure of the PWJ has received very little attention particularly in the fully developed flow regime ($x/b > 70$ (Abrahamsson, Johansson & Löfdahl 1994)). Here, x is the distance from the PWJ nozzle exit in the streamwise direction and b is the slot height (see schematic of figure 1). The term fully developed is used here to refer to the state when the streamwise mean velocity has become self-similar and the flow has become two-dimensional.

The PWJ has two shear layers, the inner boundary layer and the outer free jet (Launder & Rodi 1983) and the flow visualizations of Katz, Horev & Wygnanski (1992) suggested that the PWJ indeed contains coherent structures similar to those seen in a mixing layer and boundary layer. These flow visualizations also showed that the observed eddies extend from the wall to the outer jet region and hence the PWJ cannot be treated as two independent shear layers overlaid one on top of the other. The entire flow field is a single, interacting, wall-bounded flow with embedded structures that have similarities to those seen in free-shear layers well as

https://doi.org/10.1017/jfm.2019.559 Published online by Cambridge University Press

within boundary layers (Zhou, Heine & Wygnanski 1993, 1996). It is noted here that the specific structural characteristics of these flow eddies have yet to be described, particularly in the fully developed region of the PWJ and is the primary focus of this work.

Dejoan & Leschziner (2005) carried out a large eddy simulation (LES) of the initial PWJ development ($x/b \leqslant 22$). They confirmed that this superimposed two layer view is incomplete and the outer shear layer overlaps with the inner boundary layer in an interaction zone. The PWJ has two turbulence production peaks one in the inner wall layer and the other in the outer free-shear layer (Zhou *et al.* 1996). Dejoan & Leschziner (2005) showed that this overlap region or interaction zone occurs between the two observed production peaks. Also within this interaction zone, the turbulent production is low and the dissipation is mainly countered by turbulent transport and convection.

Dejoan & Leschziner (2005) also compared the PWJ at $x/b = 20$ with the direct numerical simulation (DNS) of a channel flow ($Re_\tau = u_\tau \delta/\nu = 180$) and observed that past the very near-wall region ($z^+ > 10$) the integral length scale across the PWJ is larger than that in the canonical boundary layer. For the purpose of this work, canonical boundary layers refers to the zero-pressure-gradient turbulent boundary layer (ZPGBL) and the fully developed turbulent channel flow (FDCF). The superscript $+$ indicates inner (viscous) normalization using the viscous length scale ν/u_τ. Here, $u_\tau = \sqrt{\tau_w/\rho}$ is the friction velocity, ν the kinematic velocity, τ_w the wall shear stress, ρ the density and δ the outer length scale which is the channel half-width in the case of the FDCF. In the case of the PWJ the outer length scale δ is the wall-normal location in the outer jet portion of the PWJ where the mean velocity is half the maximum velocity $U_{m/2}$ (see figure 1). Dejoan & Leschziner (2005) additionally observed that the integral length scale continuously increased in the wall-layer portion of the PWJ. They concluded that the outer larger scales migrate to the wall-layer through turbulent diffusion. The recent DNS study of Naqavi, Tyacke & Tucker (2018) reiterated that there exists an inner–outer interaction between the outer free-shear layer and the inner wall layer. High energy turbulence from the outer region is brought to the inner region through the triple velocity correlations while the excess energy in the inner region is transferred to the spanwise direction by the pressure–strain correlation.

Another LES study by Banyassady & Piomelli (2015) ($x/b < 35$) showed that the local streamwise Reynolds number dictates the level of intrusion of the outer scales into the inner wall layer with the intrusion being more severe at lower Reynolds numbers. Banyassady & Piomelli (2015) also noted that this observation is consistent with the theory of George *et al.* (2000) based on the asymptotic invariance principle, according to which the inner and outer layer become asymptotically independent of each other only at infinite local Reynolds number. Hence, at all finite Reynolds numbers there exists an overlap region which asymptomatically disappears at infinite Reynolds number.

The flow visualizations of Katz *et al.* (1992) indicated that the structures in the outer region are large-scale structures similar to those seen in free-shear layers. These flow structures are extremely energetic which appears as an outer peak in the streamwise turbulence intensity profile (see references in table 2 and also figure 1). These outer structures also have extremely energetic signatures while considering the spanwise and wall-normal turbulent intensities (see references in table 2).

As the wall introduces an inherent asymmetry in the case of the PWJ, the large-scale structures of a free-shear layer with inherent asymmetry, namely the mixing layer are perhaps relevant and briefly considered. The primary structure seen in a mixing

https://doi.org/10.1017/jfm.2019.559 Published online by Cambridge University Press

layer are spanwise aligned two-dimensional vortices referred to as rollers with a braid eddy between them (Rogers & Moser 1994; Loucks & Wallace 2012). It is feasible then that the outer large-scale structures seen in a PWJ are also spanwise aligned vortical structures. However, the presence of the wall must introduce changes to this structure as the wall 'blocks' these eddies while also introducing an asymmetrical mean shear (Perot & Moin 1995).

The visualizations of Katz *et al.* (1992) also suggested that the wall layer of the PWJ contains structures similar to those seen in canonical boundary layers. In addition to the outer streamwise turbulent intensity peak, the PWJ also has a peak in the wall region similar to that associated with the near-wall cycle of canonical boundary layers (Smits, McKeon & Marušić 2011). Dejoan & Leschziner (2006) used instantaneous snapshots from their LES study to show that this near-wall region of the PWJ contains streaky, streamwise, aligned structures thus showing structural similarity to canonical boundary layers. Indeed the LES based two-point correlations of Banyassady & Piomelli (2014) show elongated forward leaning large-scale structures similar to those seen in canonical boundary layers (Tutkun *et al.* 2009).

In canonical boundary layers, there is also an outer turbulence peak at high Reynolds number which is associated with large-scale structures (Samie *et al.* 2018). At lower Reynolds numbers this peak can be visualized using an appropriate filter highlighting the large scales in the flow (Smits *et al.* 2011). This outer peak in canonical layers are seen to increase with increasing Reynolds number (Smits *et al.* 2011). These large scales are classified into large-scale motions (LSM) of scale $O(\delta)$ and very large-scale motions (VLSM) or superstructures, which, as the name suggests, are extremely large flow structures with streamwise scale $O(10\delta)$ (Adrian, Meinhart & Tomkins 2000; Adrian 2007; Monty *et al.* 2009; Lee & Sung 2013). Here, in the context of a canonical boundary layer, δ refers also to the outer length scale such as the boundary-layer thickness. VLSM refers to those large-scale motions encountered in internal flows while superstructures, generally shorter than VLSM, refers to those seen in external flows (Monty *et al.* 2009).

Adrian (2007) summarizes the view that some of these large scales are formed by packets of hairpin vortices. In the buffer layers these packets are responsible for the quasi-streamwise vortices and spanwise alternating streaks of high- and low-momentum regions. These hairpins in the form of streamwise aligned packets are thought to lift and persist into the log region with decreasing frequency and have been hypothesized to be responsible for the bulges seen at the edge of the ZPGBL (Guala, Hommema & Adrian 2006; Adrian 2007; Balakumar & Adrian 2007). These packets have a streamwise scale of $O(2-3\delta)$ and are the aforementioned LSM. An alternate view of the LSM seen in the log region, based on direct numerical simulations, are that they are vortex clusters which on average occur with a sweep and an ejection (Jiménez 2012).

Observations have also been made of regions of low-speed meandering flow extending to over 10δ referred to as VLSM or superstructures (Balakumar & Adrian 2007; Hutchins & Marušić 2007*a*; Monty *et al.* 2009; Lee & Sung 2013). These low-speed regions lie in between high-speed flow regions and are predominantly seen in the logarithmic region while even extending out into the wake (Hutchins & Marušić 2007*a*; Bailey & Smits 2010). Bailey & Smits (2010), while considering proper orthogonal modes of VLSM in a pipe, show a lack of distinction between VLSM and LSM, which suggests that these two motions are interrelated. Further, their work supports the view that VLSM are formed by the alignment of multiple LSM that detach from the wall. For a different perspective, these super structures have also

https://doi.org/10.1017/jfm.2019.559 Published online by Cambridge University Press

been interpreted as global modes associated with the largest transient growth of the Orr–Sommerfeld–Squire equation by (del Álamo & Jiménez 2006).

These large-scale motions have also been observed to interact with the smaller scales of the near-wall cycle in the following manner. The large scales linearly superpose themselves on the scales of the near-wall cycle while also amplitude and frequency modulating them (Brown & Thomas 1977; Bandyopadhyay & Hussain 1984; Mathis, Hutchins & Marušić 2009*a*; Chung & McKeon 2010; Ganapathisubramani *et al.* 2012; Jacobi & McKeon 2013; Baars *et al.* 2015). Specifically, the amplitude modulation effect was observed to increase with increasing Reynolds number corresponding with the increase in the energy of the large scales (Mathis *et al.* 2009*a*). Additionally, Jacobi & McKeon (2013) show that the primary contributors to the amplitude modulation of the small scales are the VLSM.

Despite a qualitative understanding of the overall nature of the large scales within a PWJ, detailed studies focusing on the embedded structures are few and primarily LES based. This work seeks to address this gap in the literature by describing in detail the large-scale features of the PWJ. Specifically, the answers to the following questions are sought. What are the characteristics of the large-scale flow structures in the inner and outer regions of the PWJ? Do these flow features interact? Do these structures, particularly in the wall layer, have any similarities with those seen in canonical wall-bounded flows? We also seek to highlight any interaction between the large-scale and small-scale features of the flow.

The paper is organized as follows. First, experimental details are presented followed by the comparison of the present measurements with those in the literature to place the current measurements in the appropriate context. Then flow visualizations, instantaneous realizations of particle image velocimetry (PIV) velocity fields, two-point correlations and hot-wire anemometry (HWA) spectra are used to describe in detail the large-scale features of the flow. Where appropriate, direct comparisons are also made to canonical boundary layers.

2. Experimental approach

Measurements were carried out in a PWJ facility, a schematic of which is shown in figure 2. Air from a centrifugal fan passes through a series of filters and screens before entering a plenum settling chamber. From the plenum, air passes through a honeycomb layer, followed by a two-dimensional contraction of ratio 16 : 1 and exits through a rectangular nozzle. The nozzle exit has width $b = 5$ mm and an aspect ratio of 128. Past the jet exit, a 12.7 cm long trip of sandpaper (60 grit) is installed across the facility floor which trips the boundary layer. The test section of the facility is 3.66 m long with screens and honeycombs preconditioning the entrained flow as shown in the schematic of figure 2. All measurements presented in this work were carried out at a nominal jet Reynolds number $Re_j \approx bV_j/\nu \approx 5940$, where V_j is the nominal exit velocity at the centreline of the PWJ exit.

HWA measurements were carried out at several streamwise locations between $x/b = 1$ and 162. Boundary-layer type hot-wire sensors manufactured from platinum wire with diameter $d = 2.5$ μm and a nominal aspect ratio $l/d \approx 200$ were used to carry out all measurements. The hot-wire sensors were operated at an over heat ratio of 1.8. A linear encoder was used to carefully track the motion of the hot-wire sensor in the wall-normal direction. Relevant parameters of all the hot-wire measurements carried out are tabulated in table 1. For streamwise locations $x/b > 95$ the inner scaled sensing element length was ensured to be $l^+ < 10$. To fully resolve the energy of the

https://doi.org/10.1017/jfm.2019.559 Published online by Cambridge University Press

https://doi.org/10.1017/jfm.2019.559 Published online by Cambridge University Press

x/b	Re_j	V_j (ms^{-1})	U_m (ms^{-1})	u_τ (ms^{-1})	z_0^+	Re_τ	ν/u_τ (μm)	δ (cm)	l^+	l/d	TU_m/δ	ΔT^+	f_s (kHz)	f_{HW} (kHz)	f_c (kHz)
1	5964	18.06		—	—	—	—	—	—	205	—	—	20	16.7	—
50	5908	17.94	5.95	0.4009	4.34	901	38	3.47	13.5	205	72 071	0.5209	20	16.7	3.5
95	5962	17.94	4.41	0.2898	4.22	1093	53	5.76	9.9	205	36 743	0.2748	20	16.7	1.8
110	5994	17.98	4.18	0.2700	4.02	1199	56	6.77	9.8	216	25 967	0.2425	20	15.0	1.6
110	5882	17.96	3.97	0.2709	4.34	1172	57	6.71	9.1	205	42 592	0.2365	20	16.7	1.6
125	5908	17.89	3.75	0.2551	4.15	1245	60	7.51	8.6	205	29 928	0.2116	20	16.7	1.4
125	5878	17.90	3.88	0.2638	4.11	1282	59	7.52	8.9	205	30 984	0.2250	20	16.7	1.5
137	5864	17.90	3.68	0.2463	4.02	1271	63	8.00	8.3	205	33 111	0.1957	20	16.7	1.3
137*	6020	18.06	3.73	0.2471	4.20	1315	62	8.11	8.9	216	22 068	0.2002	20	15.0	1.3
137	5987	18.03	3.74	0.237	4.12	1219	65	7.87	8.5	217	19 987	0.1836	20	15.1	1.2
137	5952	17.95	3.64	0.2400	4.14	1249	64	7.97	8.6	217	21 915	0.1881	20	15.1	1.3
137	5913	18.02	3.79	0.2436	4.19	1242	64	7.90	8.7	217	23 060	0.1917	20	15.1	1.3
137	5928	18.07	3.72	0.2442	4.05	1260	63	7.99	8.7	217	22 370	0.1926	20	15.1	1.3
137	5946	18.07	3.74	0.2421	4.08	1269	64	8.09	8.6	217	22 202	0.1899	20	15.1	1.3
150	5871	17.79	3.67	0.2416	4.11	1390	64	8.85	8.7	217	27 352	0.1897	20	15.1	1.3
162	5925	17.94	3.29	0.2231	4.70	1325	69	9.14	7.6	205	25 958	0.1617	20	16.7	1.1
162	5972	18.00	3.62	0.2261	4.10	1396	68	9.46	8.1	216	18 354	0.1669	20	15.0	1.1
162	5870	17.86	3.52	0.2244	4.25	1325	69	9.12	7.5	205	25 474	0.1626	20	16.7	1.1
137	5971	18.04	—	0.2335	4.24	—	66	—	8.4	217	—	0.1776	20	15.1	1.2
137	5934	18.02	—	0.241	4.10	—	64	—	8.6	217	—	0.1881	20	15.1	1.3
137	5985	18.11	—	0.2493	4.26	—	62	—	8.9	217	—	0.2023	20	15.1	1.3
137^o	6025	18.22	3.74	—	—	—	—	7.94	—	—	—	—	—	—	—

TABLE 1. Experimental parameters from the HWA measurement campaign. Here, x is distance from the nozzle in the streamwise direction, b the jet exit height, $Re_j = V_j b/\nu$ is the jet exit Reynolds number, V_j is the jet exit velocity, ν is the kinematic viscosity, U_m is the maximum velocity, u_τ is the friction velocity, z_0^+ is the point nearest to the wall used for calculating the friction velocity, $Re_\tau = u_\tau \delta/\nu$ is the friction Reynolds number, δ is the boundary-layer thickness, ν/u_τ is the viscous length scale, l is the length of hot-wire sensing element, T is the sampling time, $\Delta T = 1/f_s$ is the sampling period, f_s is the sampling frequency of the HWA, d is hot-wire sensor diameter, f_{HW} is the estimated resonance frequency of hot-wire sensing element and $f_c = U_\tau^2/3\nu$ is the maximum flow frequency in the boundary layer as per Hutchins *et al.* (2009). The super script $+$ is used to denote non-dimensionalization using inner scales. The relevant parameters from PIV measurements at $x/b = 137$ are also shown and is indicated by the superscript ^{o}.

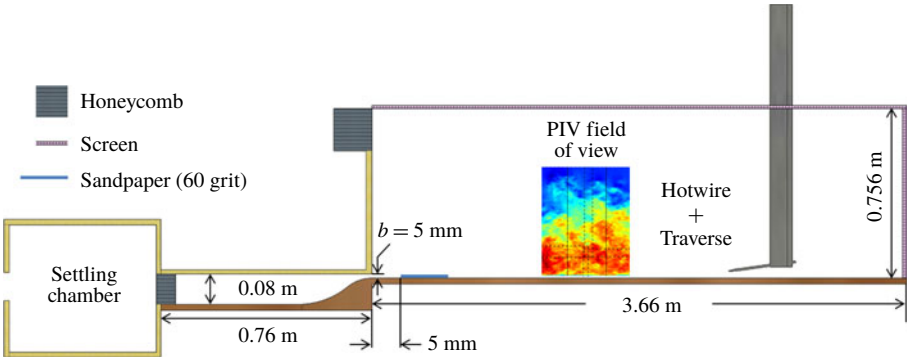


FIGURE 2. (Colour online) A schematic highlighting salient features of the experimental facility.

large scales of the flow the total sampling time was ensured to be $T > 15000\ \delta/U_m$ (Hutchins *et al.* 2009).

Measurements at certain streamwise locations were repeated as indicated in table 1. Particularly at $x/b = 137$ ten sets of measurements were carried out (seven total profiles and three near-wall region profiles) to get an estimate of the measurement uncertainty. This uncertainty is presented and discussed through the course of this paper and encompasses not only measurement errors but also changes in experimental conditions such as temperature variations.

All measurements of the total profile included 15 equally spaced points ($\approx$13 μm apart) in the very near-wall region ($z^+ < 7$ at $x/b = 137$). Outside this very near-wall region measurements were carried out at 60 logarithmically spaced wall-normal points. Points in the region $z^+ \leqslant 10$ were used to calculate u_τ as described in appendix A. While calculating u_τ all points with $z^+ < 4$ were discarded to avoid contamination due to conduction. Combined hot-wire/hot-film measurements were also carried out at a streamwise location of $x/b = 137$. A single glue-on type hot-film was used without calibration, giving an instantaneous estimate of the fluctuating wall shear stress τ_w at this streamwise location. This combined measurement was used to compute conditional velocity fields based on low-speed events of the wall shear stress.

Double-frame PIV measurements were carried out over a streamwise region centred around $x/b \approx 137$. Four cameras were used simultaneously and mosaiced together to give a single instantaneous realization of the velocity field. A 380 mJ laser, with appropriate optics, was used as the illumination source. The seeding particles were generated from mineral oil by using a fog generator, with a uniform diameter of 0.2–0.3 μm (quantified by the manufacturer). The Stokes number of the seeding particles is 0.0135. The resolution of the four cameras were identical at 6600×4400 while the images were sampled at 0.25 Hz by using an external synchronizer. The lower cameras were fitted with 200 mm micro lenses to better resolve the near-wall velocity field, resulting in a pixel resolution of $\approx$18.5 μm px^{-1}, while 105 mm micro lenses were fitted on the upper cameras, with a pixel resolution of $\approx$39.5 μm px^{-1}.

To obtain the velocity field, cross-correlation based interrogation was carried out. The initial interrogation window was 64×64 px which was decreased to 32×32 px for the final processing pass, with a 50 % overlap between windows. A typical snapshot from a single PIV realization is shown in figure 3. This single snapshot has been mosaiced using measurement from the four different cameras. The nominal fields of view (FOV) of each camera are indicated by the dashed lines in figure 3.

https://doi.org/10.1017/jfm.2019.559 Published online by Cambridge University Press

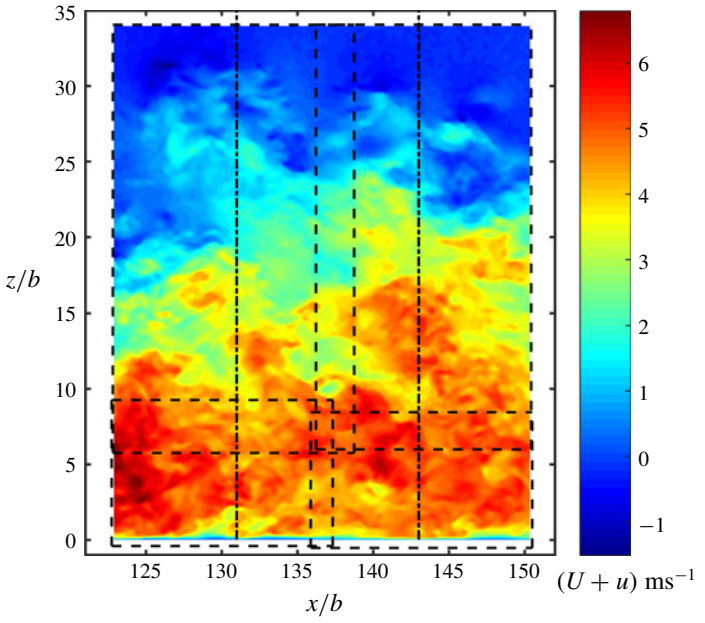


FIGURE 3. (Colour online) A typical snapshot from a single PIV realization. This realization has been mosaiced from four different cameras, the nominal field of views of which are indicated by the dashed lines (– – –).

The FOV of each individual camera was cropped to result in a nominally rectangular total FOV. The final interrogation window size of the bottom two cameras in terms of viscous units were $\Delta z^+ \times \Delta x^+ \approx 10 \times 10$ while that of the top cameras were $\Delta z^+ \times \Delta x^+ \approx 20 \times 20$. After PIV processing, the final vector field corresponding to each camera is interpolated onto a single mosaiced grid, which is then subsequently used in the analysis presented. The velocity field shown in figure 3 is one such snapshot.

The wall-normal profiles of statistical quantities derived from the PIV analysis (mean velocity, turbulent intensity etc.) are calculated by averaging across the velocity vectors over 1660 images as well as over a spatial region of $x/b = \pm 6$. This was determined to yield converged statistical quantities. Considering the streamwise position $x/b = 137$, the spatial region over which the averaging is carried out is the region between the lines (– – – – –) in figure 3. Over this region the friction velocity was estimated to vary by $\approx \pm 2\,\%$. Flow visualizations were also carried out in the PWJ facility. Theatrical smoke was used to seed the flow. A laser sheet was created using a high repetition rate laser and appropriate optics. The visualization was recorded at 1000 frames per second using a high-speed camera and the resulting movies are submitted as supplemental material available at https://doi.org/10.1017/jfm.2019.559.

The streamwise, spanwise and wall-normal ordinates are x, y and z, respectively. The streamwise and wall-normal mean velocities are U and W, respectively, while the corresponding fluctuations are u and w, respectively. It is noted the mean wall-normal velocity W is non-zero in the case of the PWJ and hence the hot-wire measures an effective mean velocity $\widetilde{U}$ and the corresponding fluctuation $\widetilde{u}$. Hence, with respect to PIV measurements $\widetilde{U} + \widetilde{u} \approx \sqrt{(U+u)^2 + (W+w)^2}$. In the case of the PWJ the outer velocity scale is the maximum velocity U_m while the outer length scale δ is

https://doi.org/10.1017/jfm.2019.559 Published online by Cambridge University Press

the location in outer jet region of the flow where the local mean velocity is half the maximum velocity i.e. $U(z=\delta)=U_m/2$ (refer to figure 1). Several past works focusing on the PWJ have been cited in this work. The relevant experimental parameters of the cited work, including the present work, are summarized in table 2.

Through the course of this work comparisons with a ZPGBL at nominally matched Re_τ are carried out. Here, $Re_\tau = \delta/(u_\tau/\nu)$ is interpreted as the ratio of the outer length scale to the inner length scale and used as the matching criterion. The PWJ measurement set used for comparison is highlighted in table 1 with the superscript *. This measurement was carried out at a streamwise location of $x/b = 137$ with $Re_\tau = 1315$. Two ZPGBL based studies were used for comparison. The ZPGBL HWA based measurements of Nugroho, Hutchins & Monty (2013) with $Re_\tau = 1308$ and the DNS of Sillero, Jiménez & Moser (2013) at $Re_\tau = 1307$ were used.

3. Results

3.1. *Two-dimensionality and friction velocity* u_τ

The friction velocity u_τ was calculated using a near-wall fit of the streamwise velocity profile and the details of the technique are described in appendix A. In this section the friction velocity measurements are compared with those in the literature. In the review of Launder & Rodi (1981), while assessing PWJ experimental data, the two-dimensionality of the flow field was used as a key criterion. Hence, the two-dimensionality of the current flow field is also assessed using the two-dimensional, streamwise momentum integral equation. In the case of the PWJ the two-dimensional momentum integral equation (Eriksson *et al.* 1998; George *et al.* 2000) is

$$\int_0^\infty (U^2 + \overline{u^2} - \overline{w^2})\,\mathrm{d}z = M_r - \int_{x_r}^x u_\tau^2\,\mathrm{d}x, \tag{3.1}$$

where M_r is the momentum added to the control volume at some upstream, streamwise reference location x_r. Defining

$$M_j = \int_0^\infty (U^2 + \overline{u^2} - \overline{w^2})\,\mathrm{d}z, \quad \text{and} \quad M_\tau = \int_{x_r}^x u_\tau^2\,\mathrm{d}x \tag{3.2a,b}$$

equation (3.1) can we rewritten as

$$\frac{M_j}{M_r} = 1 - \frac{M_\tau}{M_r}. \tag{3.3}$$

Equation (3.3) states that the loss in momentum of the jet M_j is balanced by the losses due to wall friction M_τ. Figure 4(*a*) shows the variation of the friction coefficient based on the jet exit velocity $C_{fj} = 2u_\tau^2/(V_j^2)$ as a function of downstream distance x/b. An error bar showing one standard deviation on either side of the mean is shown at the streamwise location $x/b = 137$. The curve fit shown in figure 4(*a*) is then integrated to calculate M_τ along with an estimated propagation error.

Figure 4(*b*) shows the left- (M_j/M_r) and right- $(1 - M_\tau/M_r)$ hand terms of the momentum integral equation (3.3) as evaluated using HWA measurements. These are shown as a function of streamwise location x/b. Due to the use of the sandpaper trip and the difficulty in carrying out near-wall $(z^+ < 10)$ velocity measurements very close to the jet exit (smaller viscous length scale), the reference location used is $x_r/b = 95$. It is again noted that M_j from the HWA measurements was evaluated using effective

https://doi.org/10.1017/jfm.2019.559 Published online by Cambridge University Press

https://doi.org/10.1017/jfm.2019.559 Published online by Cambridge University Press

References	Re_j	x/b_{max}	V technique	u_τ technique	%TI_{exit}	Symbols
Wygnanski *et al.* (1992), Zhou *et al.* (1996)	5000–19 000	140	SHWA, XHWA	LNWF		◇
Karlsson, Eriksson & Persson (1993*a*,*b*)	9600	200	LDV	LNWF	0.9	○
Schneider & Goldstein (1994)	14 000	108	LDV		0.3	▼
Abrahamsson *et al.* (1994)	10 000–20 000	150	SHWA, XHWA	PT	0.4	▷
Eriksson, Karlsson & Persson (1998)	9600	150	LDV	NWF	1	□
Venås *et al.* (1999)	10 000	150	PHWA, XHWA		0.4	▶
Schober & Fernholz (2000)	10 000	200	SHWA, XHWA	PT, SF, WHW		■
Tachie, Balachandar & Bergstrom (2002, 2004)	7500–14 000	130	LDV	GCF	3–5	☆
Ahlman, Brethouwer & Johansson (2007)	2000	40	DNS			△
Smith (2008)	20 000–46 000	170	HWA	Corr		▲
Dunn (2010)	8100	100	PIV		1.45	◀
Rostamy *et al.* (2011*a*,*b*)	7500	80	LDV	GCF, LL	0.7	◁
Banyassady & Piomelli (2014, 2015)	1100–40 000	40	LES			▽
Dejoan & Leschziner (2005, 2006, 2007)	9600	22	LES			
Naqavi *et al.* (2018)	7500	40	DNS			
Current	5940	162	SHWA PIV	NWF	<1	×, ——, – – –, – – – – – +, ——, – – —

TABLE 2. Summary of parameters of major PWJ work cited including present work. Associated works are summarized together. Abbreviations used are as follows: SHWA, single hot-wire anemometry, XHWA, cross hot-wire anemometry, PHWA, pulsed hot-wire anemometry LDV, laser Doppler velocimetry, PIV, particle image velocimetry, LNWF, linear near-wall fit, PT, Preston tube, SF, surface fence, WHW, wall hot-wire, GCF, curve fit of near-wall region as proposed by George *et al.* (2000), LL, log law, Corr, correlation of C_f versus Re_m of George *et al.* (2000), NWF, near-wall fit, MB, momentum balance and TI_{exit}, turbulent intensity at jet exit, DNS, direct numerical simulation.

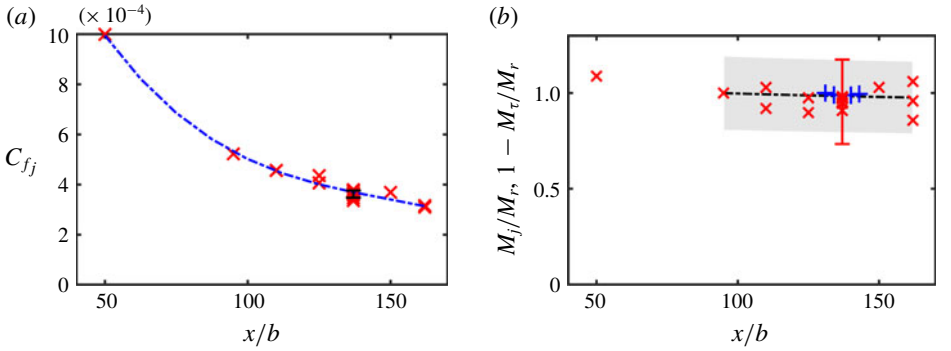


FIGURE 4. (Colour online) (*a*) The variation of the friction coefficient $C_{f_j} = 2u_\tau^2/(V_j^2)$ as a function of downstream distance x/b. The error bar at $x/b = 137$ shows one $\pm$ standard deviation in the measurement of u_τ. The line (– – – –) is a curve fit of C_{f_j} versus x/b. (*b*) The balance between the left side M_j/M_r ($\times$) and right side $1 - M_\tau/M_r$ (– – –) of (3.3) at various streamwise locations. Here M_r is evaluated at $x_r/b = 95$. The left side terms as calculated using PIV velocity profiles are also shown (+). In this case M_r is evaluated at $x_r/b = 131$. The shaded area is a conservative estimate of the propagation error associated with the calculation of the integral ratio M_τ/M_r while the error bar is that associated with the calculation of the ratio M_j/M_r.

quantities $\widetilde{U}^2$ and $\widetilde{\overline{u^2}}$. Also shown in figure 4(*a*) is the left-hand side of (3.3) (M_j/M_r) calculated using PIV measurements. In this case all three terms in (3.3) (U^2, $\overline{u^2}$ and $\overline{w^2}$) are used to evaluate M_j while $x_r/b = 131$.

The shaded area in figure 4(*b*) is a conservative estimate of the propagation error associated with the calculation of the integral ratio M_τ/M_r while the error bar is that associated with the calculation of the ratio M_j/M_r. Based on figure 4(*a*) it is clear that the two-dimensional momentum equation is satisfied between $95 < x/b < 162$ and the flow is thus considered two-dimensional in this region. Further the agreement between the PIV and HWA based evaluations is also evident.

The variation of the friction coefficient based on the outer velocity scale $C_{f_m} = 2u_\tau^2/(U_m^2)$ as a function of the local Reynolds number $Re_m = z_m U_m/\nu$ is shown in figure 5(*a*). Various measurements from the literature are shown for comparison (black symbols). The fit of Bradshaw & Gee (1960) $C_{f_m} = 0.0315 Re_m^{-0.182}$ based on Stanton tube measurements is also shown. Hammond (1982) developed an optimum log law for the skin friction of a PWJ, $C_{f_m} = 0.0667 Re_m^{-0.258}$, which is also shown.

The current measurements of C_{f_m} are higher than the Stanton tube and Preston tube based measurements (Bradshaw & Gee 1960; Abrahamsson *et al.* 1994), as well as those measurements from near-wall LDV based nonlinear curve fits (Karlsson *et al.* 1993*b*; Eriksson *et al.* 1998; Tachie *et al.* 2002). The present measurements are significantly higher than those measured using a linear near-wall curve fit using HWA measurements (Wygnanski *et al.* 1992). However, it is in good agreement with the LES of Banyassady & Piomelli (2015) as well as the log law of Hammond (1982). Wygnanski *et al.* (1992), following the work of Narasimha, Narayan & Parthasarathy (1973), showed that when non-dimensionalized using the jet influx momentum J there is excellent collapse of u_τ verses the non-dimensional streamwise distance (after correcting for the virtual origin x_0), over a range of Reynolds numbers. The current measurements are compared with the curve fit proposed by Wygnanski *et al.* (1992) in figure 5(*b*). Also shown are the experimental results of Wygnanski *et al.* (1992) at

https://doi.org/10.1017/jfm.2019.559 Published online by Cambridge University Press

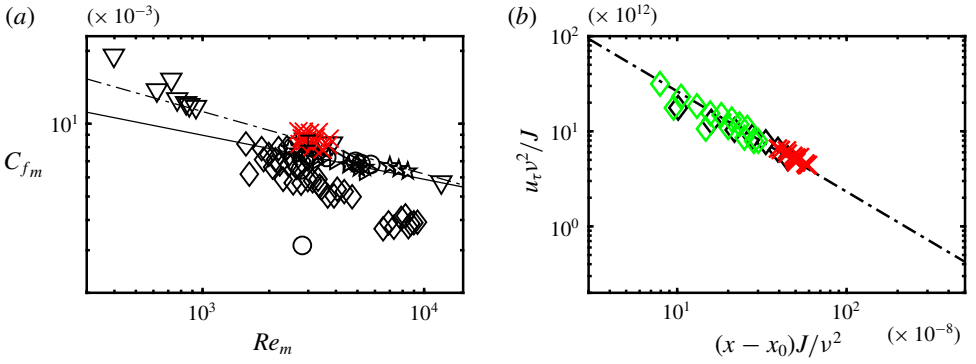


FIGURE 5. (Colour online) (*a*) The variation of the local skin friction coefficient $C_{f_m} = 2u_\tau^2/(U_m^2)$ as a function of the local Reynolds number $Re_m = z_m U_m/\nu$ of the present measurements (×). The black symbols correspond to various measurements from prior work (refer to table 2 for symbols). Also shown are the fit of Bradshaw & Gee (1960) $C_{f_m} = 0.0315 Re_m^{-0.182}$ (——) and the log law $C_{f_m} = 0.0667 Re_m^{-0.258}$ of Hammond (1982) (– – – –). (*b*) Compares the present measurements of u_τ (×), non-dimensionalized by the jet momentum J with the curve fit of Wygnanski *et al.* (1992) (– – – –). Comparisons are made with the measurements from Wygnanski *et al.* (1992) at $Re_j = 5000$ (◇, green) and 7000 (◇).

PWJ Reynolds numbers $Re_j = 5000$ and 7500. The current measurements agree well with both the measurements and the curve fit of Wygnanski *et al.* (1992).

3.2. *Inner-scaled mean velocity profile*

Figure 6(*a*) shows the inner-scaled effective mean velocity $\widetilde{U}$ profile from HWA measurements. Also shown are the PIV based profiles of the streamwise mean velocity U and the wall-normal mean velocity W. All these profiles were measured at a streamwise location of $x/b = 137$. Also shown for comparison is the mean streamwise velocity profile from the ZPGBL measurements of Nugroho *et al.* (2013). The traditional log law is,

$$U^+ = \frac{1}{\kappa} \ln z^+ + A, \tag{3.4}$$

where the constants κ and A are dependent on the flow geometry (Chauhan, Monkewitz & Nagib 2009; Marušić *et al.* 2010). Shown in figure 6(*a*) are two lines with different κ and A, one with $\kappa = 0.384$ and an intercept of $A = 4.17$ which corresponds to the ZPGBL measurements of Nugroho *et al.* (2013). The other was drawn with $\kappa = 0.41$ and an intercept $A = 4$. There is considerable spread in reported values of κ and A for a PWJ. A majority of the works report a value of $\kappa = 0.41$ (Abrahamsson *et al.* 1994; Eriksson *et al.* 1998; Tachie *et al.* 2002; Rostamy *et al.* 2011*b*) while values as low as 0.182 have also been reported (Wygnanski *et al.* 1992). The reported values of the intercept A ranges from 5.0 (Abrahamsson *et al.* 1994; Eriksson *et al.* 1998; Tachie *et al.* 2002; Rostamy *et al.* 2011*b*) to 9.5 (Wygnanski *et al.* 1992). Wygnanski *et al.* (1992) also report an intercept A which varies with jet Reynolds number in contrast with a majority of other work.

The DNS of Ahlman *et al.* (2007) indicate an identical inner near-wall region ($z^+ < 10$, see figure 25*a*) for all streamwise locations considered (simulations carried

https://doi.org/10.1017/jfm.2019.559 Published online by Cambridge University Press

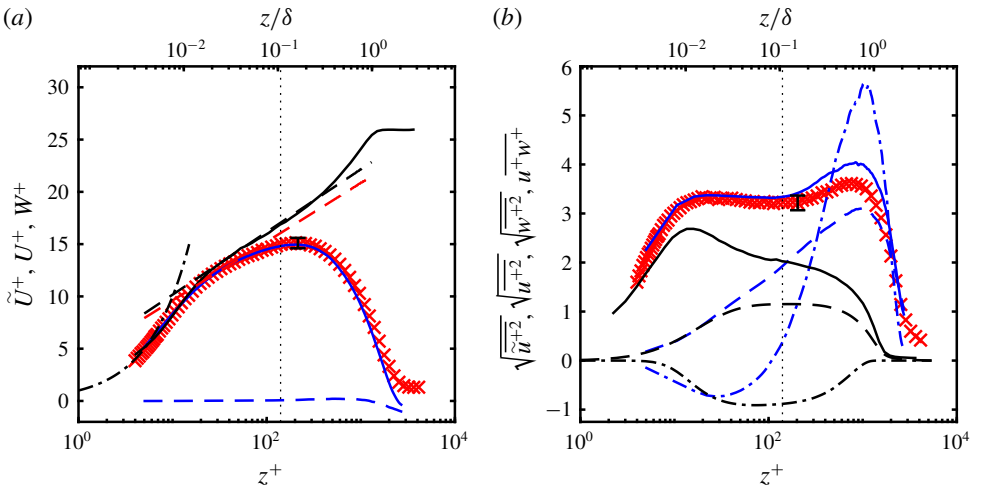


FIGURE 6. (Colour online) (*a*) The inner-scaled mean velocity profile of the PWJ as measured by HWA (×) along with the PIV based streamwise mean velocity U (——, blue) and the wall-normal mean velocity W (– – –, blue). These measurements were carried out at $x/b = 137$. Also shown at matched Re_τ is the profile corresponding to the ZPGBL measurements of Nugroho *et al.* (2013) (——). Note, Nugroho *et al.* (2013) use $\delta = \delta_{98}$ as the outer scale which is followed while presenting their data. Two log-law profiles are shown, one with $\kappa = 0.384$, $A = 4.17$ (– – –, black) and the other with $\kappa = 0.41$, $A = 4$ (– – –, red). Also shown is the profile corresponding to $U^+ = z^+$ (– – – –). (*b*) Turbulent stress profiles of the PWJ are presented. HWA based stress $\sqrt{\widetilde{u^{+2}}}$ (×), PIV based stresses $\sqrt{\overline{u^{+2}}}$ (——, blue), $\sqrt{\overline{w^{+2}}}$ (– – –, blue) and $\overline{u^+w^+}$ (– – – –, blue) at $x/b = 137$ are shown. Comparisons are also made with a ZPGBL at matched Re_τ i.e. the HWA based streamwise turbulent intensity $\sqrt{\overline{u^{+2}}}$ (——, black) (Nugroho *et al.* 2013) and the DNS based stresses $\sqrt{\overline{w^{+2}}}$ (– – –), $\overline{u^+w^+}$ (– – – –) (Sillero *et al.* 2013).

out up to $x/b = 40$). However the mean velocity profile appears to indicate a variation in κ and A with downstream distance. These constants depend on the accurate measurement of u_τ and it is not surprising in that regard to see the spread in the reported values of κ and A, considering the large spread in the literature as seen in figure 5(*a*). Banyassady & Piomelli (2015) show based on their LES study that these constants appear to depend on the local Reynolds number Re_m which is an artefact of the intrusion of the outer jet region into the inner wall region. They conclude that the variation in reported constants can be attributed to different local Reynolds numbers and at large enough values $Re_m > 5200$ these constant will approach $\kappa = 0.41$ and $A = 5.2$.

3.3. *Turbulent stresses*

The inner-scaled turbulent intensity profiles are shown in figure 6(*b*) along with the corresponding profile from the ZPGBL measurements of Nugroho *et al.* (2013). The inner-scaled wall-normal turbulent intensity as well as the Reynolds stress profiles from the ZPGBL DNS of Sillero *et al.* (2013) are also shown. The streamwise turbulent intensity $\sqrt{\overline{u^{+2}}}$ from the PIV based measurements show a higher intensity

https://doi.org/10.1017/jfm.2019.559 Published online by Cambridge University Press

than the effective turbulent intensity $\sqrt{\widetilde{u^{+2}}}$ as measured by HWA in the outer regions of the PWJ ($z/\delta > 0.1$). This is consistent with the measurement technique used as there are instantaneous flow reversals in the outer extremities of the PWJ which results in a higher intensity measured by PIV.

When compared with a ZPGBL the streamwise turbulent intensities of the PWJ are higher across the entire layer. The streamwise turbulent intensity of the PWJ increases rapidly in the near-wall region ($z^+ < 10$) and reaches almost a plateau at $z^+ \approx 16$ which corresponds to the near-wall peak seen in canonical boundary layers. The streamwise intensity of the PWJ then marginally decreases and then increases again to reach a peak at $z/\delta \approx 0.7$ which corresponds to the turbulent activity in the outer shear layer. The inner-scaled spanwise turbulent intensity $\sqrt{\overline{w^{+2}}}$ of the PWJ is virtually identical to that of the ZPGBL DNS up to $z^+ > 30$ beyond which it increases rapidly reaching a peak in the outer jet region much like the streamwise turbulent intensity. The peak streamwise turbulent intensity is approximately three times the inner-scaled turbulent intensity of the ZPGBL indicative of the large wall-normal turbulent activity particularly in the outer region of the PWJ. The inner-scaled Reynolds shear stress $\tau_{uw}^{+} = -\overline{u^{+}w^{+}}$ of the PWJ (the negative of which is plotted in figure 6) in the near-wall region increases in a manner that is similar but not identical to the ZPGBL and reaches a maximum at about $z^+ \approx 30$ following which it also rapidly decreases to a large negative peak in the outer jet region.

There is also considerable spread in the literature in the peak turbulent intensity levels measured in various PWJ facilities. Rostamy *et al.* (2011*a*) compare the outer-scaled peak streamwise turbulent intensity measurements from several sources and present strong evidence that it is a function of the jet Reynolds number Re_j. As part of the present work a similar comparison was made and is shown in figure 7(*a*). In addition, the peak outer-scaled wall-normal turbulent intensities as well as the outer-scaled peak Reynolds shear stresses are compared. In figures 7(*b*) and 8, the complete profiles have also been compared with the closest available jet Reynolds numbers in the literature i.e. $Re_j = 5000$ (Wygnanski *et al.* 1992) and 7500 (Rostamy *et al.* 2011*a*). It is noted that a majority (not all) of the previous studies (Abrahamsson *et al.* 1994; Schneider & Goldstein 1994; Eriksson *et al.* 1998) show outer-scaled stress profiles converging to a self-similar one at streamwise distances $x/b \gtrsim 70$ for a given jet Reynolds number. Nominal error bars of $\pm 4\,\%$ are shown in figure 7(*a*) to indicate the statistical significance of the variation. It is clear that all three peak stresses decrease with an increase in Reynolds number. This is consistent with the conclusions of Banyassady & Piomelli (2015) as stated in the section discussing the log-law constants. As there are two differently scaled sources of turbulence within a PWJ, in addition to being a boundary layer and a jet it also is a mixing layer. The large wall-normal turbulent intensity in a PWJ also supports this argument of mixing layer like behaviour in a PWJ. Hence, if there is less interaction between the two layers with increasing Reynolds number, as suggested by Banyassady & Piomelli (2014), this will indeed result in lower intensity levels. In addition to the jet Reynolds number there are significant differences in the facilities used in past studied. For example, water facilities (Eriksson *et al.* 1998) have a bounding free surface. It is possible that variations in experimental set-ups are also an additional contributing factor to this variation in turbulent intensities. Further, as there are significant instantaneous flow reversals in the outer free jet portion, HWA based measurements underestimate the peak turbulent intensities.

https://doi.org/10.1017/jfm.2019.559 Published online by Cambridge University Press

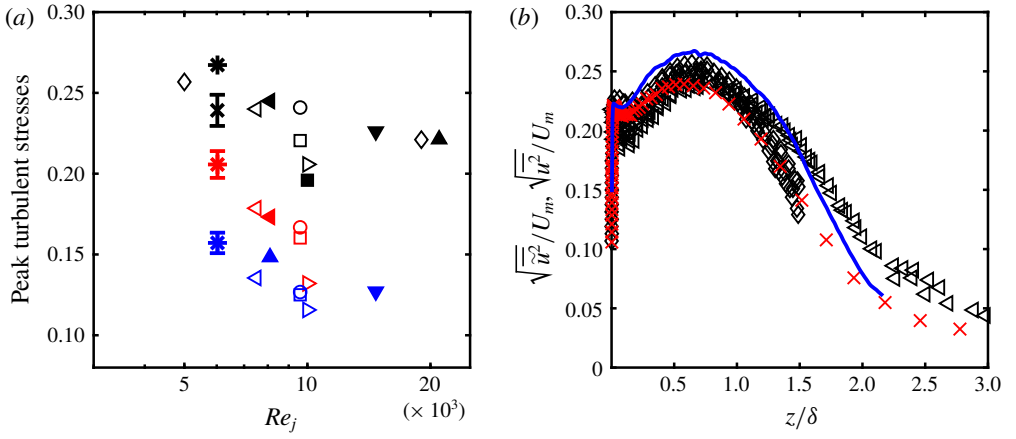


FIGURE 7. (Colour online) (*a*) Compares the peak turbulent intensities as a function of the jet Reynolds number Re_j. The closed symbols are the present measurements while the open ones are from the literature (see table 2 for symbols). The black symbols are the peak non-dimensionalized streamwise turbulent intensities ($\sqrt{\widetilde{\overline{u^2}}}/U_m$ or $\sqrt{\overline{u^2}}/U_m$), the red ones the peak wall-normal turbulent intensities ($\sqrt{\overline{w^2}}/U_m$) while the blue ones are the peak cross stresses ($\sqrt{\overline{uw}}/U_m$). (*b*) Compares the streamwise turbulent intensity profiles as measured by HWA $\sqrt{\widetilde{\overline{u^2}}}/U_m$ (×) and PIV $\sqrt{\overline{u^2}}/U_m$ (——), with those from the literature (see table 2 for symbols).

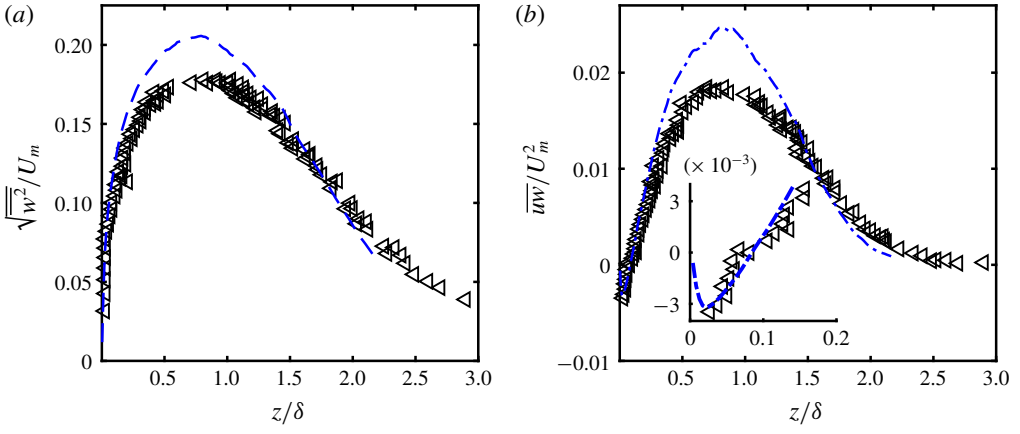


FIGURE 8. (Colour online) Comparison of the (*a*) wall-normal turbulent intensity profiles $\sqrt{\overline{w^2}}/U_m$ (– – –) and (*b*) negative Reynolds shear stress profile $\overline{uw}/U_m^2$ (– – – –) of the present PWJ with those from past studies (see table 2 for symbols). The inset of (*b*) shows a zoomed in view of the Reynold shear stress profile at the wall-normal location where $\overline{uw}$ changes sign.

3.4. *Shear stress, production and dissipation*

The shear stress profile τ, in the PWJ is shown in figure 9(*a*). Here the total shear stress τ is divided into its viscous and Reynolds components given by

$$\tau = \tau_{uw} + \tau_{visc} = -\overline{uw} + \nu \frac{\partial U}{\partial z}. \tag{3.5}$$

https://doi.org/10.1017/jfm.2019.559 Published online by Cambridge University Press

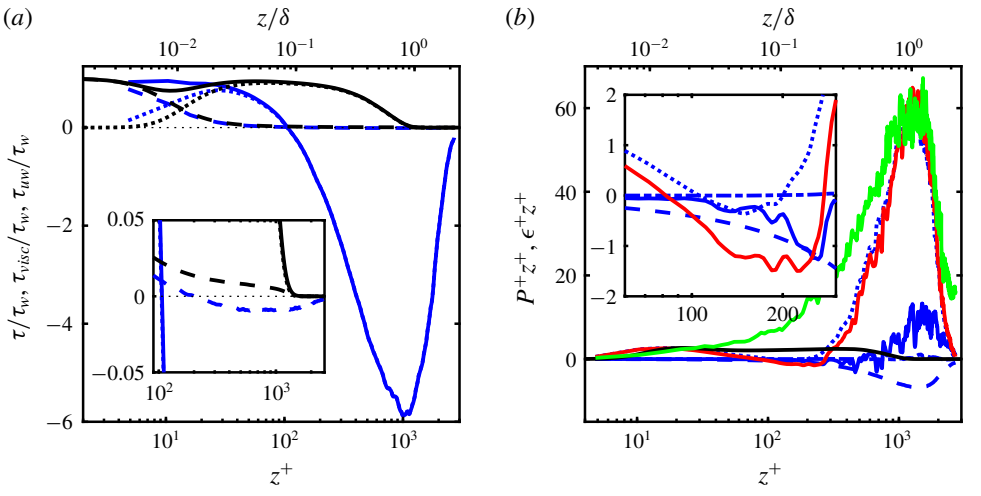


FIGURE 9. (Colour online) (*a*) Profiles of the non-dimensionalized viscous stress τ_{visc} (– – –), Reynolds stress τ_{uw} (- - - - - -) and the total stress τ (——, blue) across the PWJ are shown. The corresponding lines in black are the matched ZPGBL profiles from the DNS of Sillero *et al.* (2013). (*b*) Profiles of the contributors to the turbulent production in the PWJ according to (3.6), are shown in pre-multiplied form. The various lines are P (——, red), P_1 (- - - - - -), P_2 (– – –), P_3 (——, blue) and P_4 (– – – – –). $P \approx P_1$ in pre-multiplied form corresponding to the ZPGBL DNS of Sillero *et al.* (2013) (——). The pre-multiplied dissipation rate in the PWJ according to (3.7) (——, green) is also shown.

Also shown for comparison are τ, τ_{visc} and τ_{uw} corresponding to the ZPGBL DNS of Sillero *et al.* (2013). In the PWJ τ_{visc} crosses τ_{uw} at $z^+ \approx 11$ while in the ZPGBL this occurs at $z^+ \approx 13$. These are in good agreement with each other and also the ZPGBL measurements of De Graaff & Eaton (2000) who reported a crossing at $z^+ \approx 10$. In both the PWJ and ZPGBL, τ_{visc} reduces to near zero in a very similar manner. However, as shown in the inset of figure 9(*a*), in the case of the PWJ the viscous stress τ_{visc} is at a value that is very close to zero but has a low negative value due to the change in sign of the velocity gradient in the outer jet portion of the PWJ. The Reynolds shear stress τ_{uw} of the PWJ changes sign at $z^+ \approx 100$ or $z/\delta \approx 0.1$ (see inset of figure 8*b*) after which it decreases rapidly, to a large negative maximum of around $-6\tau_w$.

The inner-scaled turbulent production P^+ in the case of the PWJ and canonical boundary layers reduces to

$$P^+ = \underbrace{-\overline{u^+w^+}\frac{\partial U^+}{\partial z^+}}_{P_1} \underbrace{-\overline{u^{+2}}\frac{\partial U^+}{\partial x^+}}_{P_2} \underbrace{-\overline{w^{+2}}\frac{\partial W^+}{\partial z^+}}_{P_3} \underbrace{-\overline{u^+w^+}\frac{\partial W^+}{\partial x^+}}_{P_4}. \tag{3.6}$$

In a canonical boundary layer with or without a pressure gradient, considering each of these four terms, P_1 is of order $O(10^{-1})$, P_2 and P_3 are of order $O(10^{-4})$ while P_4 is of order $O(10^{-6})$ (Harun *et al.* 2013). Hence, P_1 is the only non-negligible term and is plotted for the ZPGBL DNS of Sillero *et al.* (2013) in figure 9(*b*). This is plotted in inner-scaled pre-multiplied form P^+z^+ to ensure equal areas contribute equally to the production. Also plotted are all four terms of P^+z^+ of the PWJ calculated using

https://doi.org/10.1017/jfm.2019.559 Published online by Cambridge University Press

PIV measurements. The most dominant and relevant term across the PWJ is also P_1 and is used to approximate the total production.

Both the PWJ and the ZPGBL have inner peaks of turbulent production in the near-wall region. At $x/b = 137$ the inset of figure 9(*b*) shows a region of negative P^+z^+ between $z^+ \approx 90$ and $z^+ \approx 250$ while $z^+(U_m) \approx 200$. We note that these profiles were calculated using numerical differentiation which are susceptible to large propagation errors. Hence, it is only safe to conclude that the production in this region is very low.

Above this inner region there is a large increase in P^+z^+, reaching a maximum of around $P^+z^+ \approx 60$ which is more than twenty times the inner peak. Therefore there is a large increase in outer P^+z^+ with no apparent difference in the inner P^+z^+ peak, when comparing with a matched ZPGBL. This suggests that the flow features producing the large turbulent kinetic energy in the outer region is inactive in the sense of Townsend (Townsend 1976). In other words, these outer layer flow structures do not contribute to $-\overline{uw}$ in the near-wall region though they do contribute to $\overline{u^2}$.

As a relevant aside, Zhou *et al.* (1996) studied a PWJ in an external stream with a velocity that was 8 % of the maximum PWJ velocity. The PWJ Reynolds number was close to the present jet Reynolds number at $Re_j = 6900$. They also observed a large peak in the production in the outer region however this outer peak was smaller than the inner one. This indicates that the structures associated with this peak are free-shear layer type structures. Zhou *et al.* (1996) did not observe a region of negative turbulent production between the inner and outer peaks though the overall production in this region was very close to zero. However, in other past works of PWJ with an external stream the production appears to become negative in this region (works cited by Irwin (1973)). It is also noted that the LES of Dejoan & Leschziner (2005) shows a region of very low but positive production between the two production peaks.

Assuming that the turbulence is isotropically dissipated the dissipation rate ϵ reduces to (Zhou *et al.* 1996)

$$\epsilon = 15\nu\overline{\left(\frac{\partial u}{\partial x}\right)^2}. \tag{3.7}$$

The dissipation rate profile of the PWJ at $x/b = 137$, calculated using (3.7) from PIV measurements, is shown in pre-multiplied form in figure 9(*b*). It is clear that most of the energy is dissipated at the wall-normal locations $z^+ > 100$. Shown in figure 10 is the ratio of the production to dissipation P/ϵ across the PWJ. The production exceeds the dissipation in the near-wall region while in the outer region there is a region where P/ϵ is close to unity ($z^+ \approx 1000 - 1700$, $z/\delta \approx 0.8 - 1.36$). Particularly in the limited log region (around $z^+ \approx 140$) the flow is not in equilibrium in contrast to canonical boundary layers (Pope 2001). The dissipation rate is considerably larger than the production at wall-normal locations $z^+ \approx 30 - 300$ ($z/\delta \approx 0.026 - 0.24$). This suggests that there is a spatial transport of turbulent energy from regions above and below to the region of low turbulent production ($z^+ \approx 30 - 300$). These observations are consistent with the LES study of Dejoan & Leschziner (2005). This region has been broadly referred to as the overlap region or interaction zone. However, the recent DNS study concludes that turbulent energy is transported to the near-wall region from the outer region, with the excess energy being transferred in the spanwise direction (Naqavi *et al.* 2018).

https://doi.org/10.1017/jfm.2019.559 Published online by Cambridge University Press

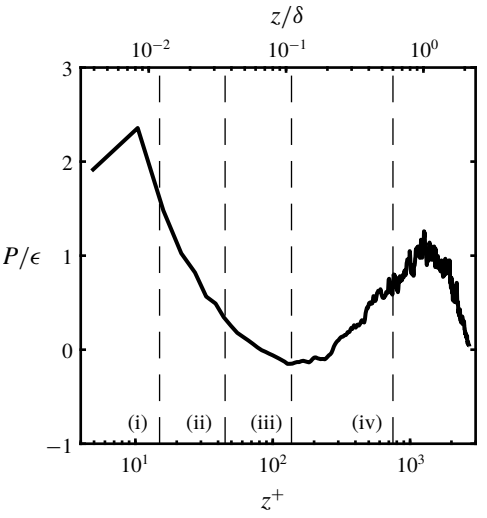


FIGURE 10. The distribution of the estimated production to dissipation rate within the PWJ at $x/b = 137$.

3.5. *Energy spectra*

A closer look at the energy spectra is now presented to get an estimate of the scale and associated energy of the flow structures within a PWJ. The one-dimensional pre-multiplied energy spectrum of the inner-scaled streamwise effective velocity $k_x^+\phi_{\widetilde{uu}}^+$ as measured by HWA at $x/b = 137$ is shown in figure 11(*a*) while that of the matched ZPGBL measurements of Nugroho *et al.* (2013) is shown in figure 11(*d*). The pre-multiplied streamwise $k_x^+\phi_{uu}^+$ and spanwise $k_x^+\phi_{ww}^+$ energy spectra as measured using PIV are shown in figures 11(*b*) and 11(*c*) respectively. In the case of the HWA based spectra a frequency has been converted to streamwise wavelength λ_x using Taylor's frozen hypothesis where the local mean velocity was used as the convection velocity. The PIV based measurements reflect the actual wavelength components. However, in the case of the PIV based measurements, due to the finite FOV, the scales larger than the streamwise extent of the FOV are unresolved and leak into the first few wavenumber components. For this reason the first three wavenumber components of the PIV based spectra of figures 11 and 12 have been removed. It is also noted that in figure 11 the colour contour levels of $k_x^+\phi_{uu}^+$ corresponding to the ZPGBL, are half of those reflected by the colour bar.

The symbol $\times$ in figure 11(*a*,*d*) mark the location of the inner peak ($\lambda_x^+ \approx 1000$, $z \approx 15^+$) as identified in canonical boundary layers (Hutchins & Marušić 2007*b*; Monty *et al.* 2009). This inner peak of canonical layers corresponds to the inner production peak seen in figure 9(*b*) and is associated with the near-wall cycle of quasi-streamwise vortices or streaks (Kline *et al.* 1967; Hutchins & Marušić 2007*b*). An outer peak is also seen in canonical boundary layers at the approximate geometric centre of the logarithmic region i.e. $z^+ \approx \sqrt{15Re_\tau}$, at wavelengths $\lambda_x \approx 6\delta$. This peak was observed to increase in magnitude with increasing Re_τ (Mathis *et al.* 2009*a*). This location is identified in figure 11(*a*,*d*) by the symbol $+$. Four sets of line plots of the pre-multiplied spectra are also shown in figure 12. Each of the plots correspond to slices of figure 11 at four wall-normal locations as indicated by the white dashed lines of figure 11. The four locations are (i) $z^+ \approx 15$, which corresponds to the location of the

https://doi.org/10.1017/jfm.2019.559 Published online by Cambridge University Press

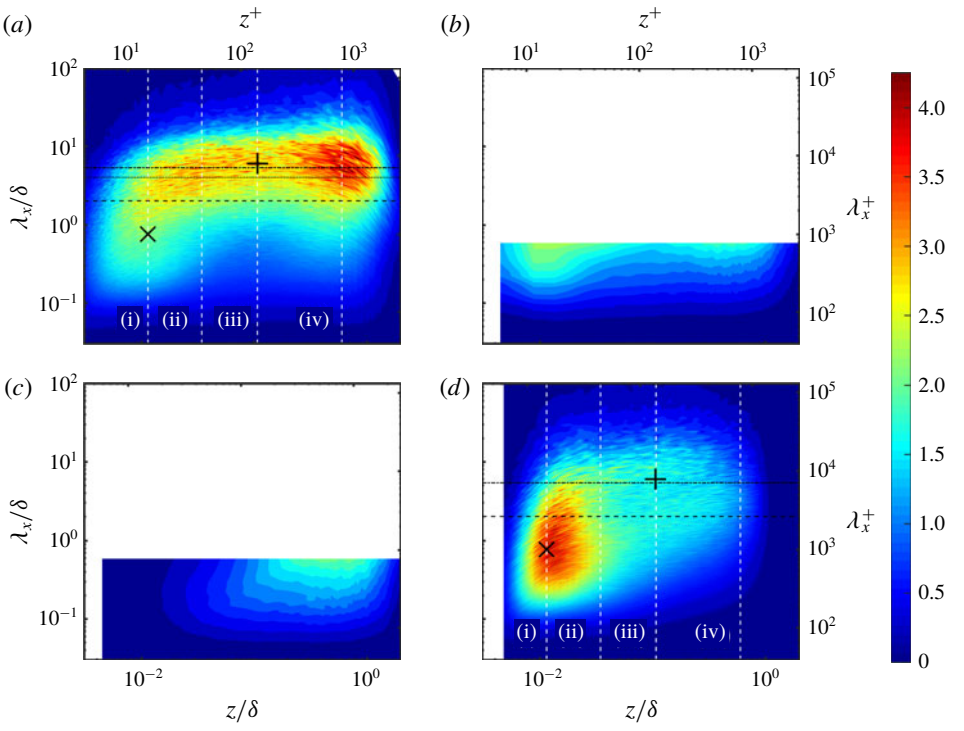


FIGURE 11. (Colour online) Colour contours of the inner-normalized one-dimensional pre-multiplied spectra of the PWJ as measured by (*a*) HWA $k_x\phi_{\widetilde{uu}}$, (*b*) PWJ streamwise spectra $k_x\phi_{uu}$ (PIV based) and (*c*) spanwise spectra $k_x\phi_{ww}$ (PIV based) and (*d*) the corresponding matched ZPGBL spectra $k_x\phi_{uu}$ as measured by Nugroho *et al.* (2013). Note – the colour contours of (*d*) are at 50 % of that indicated by the colour bar. The location of the inner peak at $z^+ \approx 15$, $\lambda_x \approx 1000$ (×) as well as the location $z^+ \approx \sqrt{15Re_\tau}$, $\lambda_x \approx 6\delta$ (+) are highlighted. Please note that the PIV-based panels (*b*) and (*c*) display partial plots showing only the wavelengths resolved by the PIV field of view as described in the main text.

inner peak in canonical boundary layers, (ii) $z^+ \approx 45$, (iii) $z^+ \approx \sqrt{15Re_\tau}$ and finally (iv) $z^+ = 0.6Re_\tau$ which corresponds to the centre of the energetic outer peak seen in the PWJ (see figure 11*a*). The three locations closest to the wall are all less than z_m, the location of the maximum velocity U_m. The corresponding locations are also shown in the production to dissipation plot of figure 10. The outer peak in the case of the ZPGBL data of Nugroho *et al.* (2013) has a weak signature as seen in the line plot of figure 12(*c*). The inner and outer peak are not distinctly visualized in the case of the PWJ.

A suitable threshold to broadly distinguish large scales from small scales in a canonical boundary layer, at sufficiently large $Re_\tau > 3500$, is $\lambda_x^+ = 7000$ i.e. the small scales in the flow are those with $\lambda_x^+ < 7000$ and the large scales are those above this threshold (Mathis, Hutchins & Marušić 2011*a*; Pathikonda & Christensen 2017). At lower Re_τ, due to insufficient scale separation, other cutoffs have been used, the most common one being $\lambda_x = \delta$ (Mathis *et al.* 2009*b*; Harun *et al.* 2013). Shown in figure 11(*a*,*d*) are the lines corresponding to $\lambda_x^+ = 7000 = 5.3\delta$, $\lambda_x = 2\delta$ and $\lambda_x = 4\delta$. In the case of the PWJ it is clear that there is significant large-scale energy in the outer layer at $\lambda_x^+ = 7000$. In a ZPGBL Kulandaivelu (2011) has shown

https://doi.org/10.1017/jfm.2019.559 Published online by Cambridge University Press

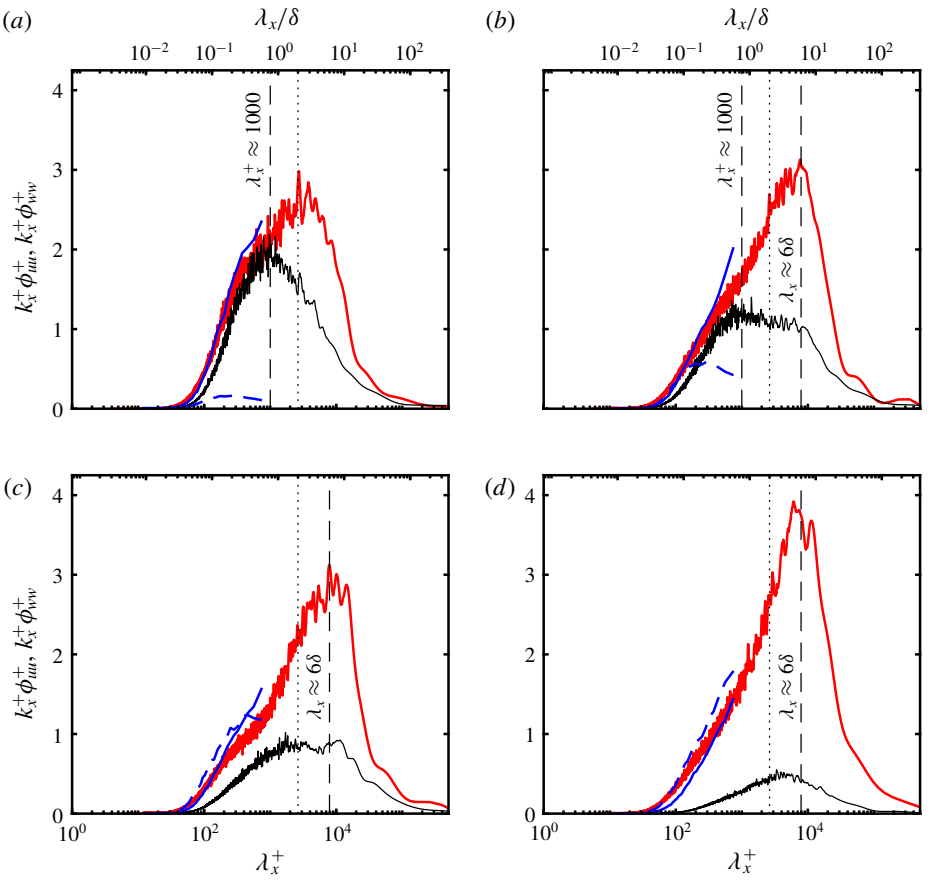


FIGURE 12. (Colour online) Line plots of the inner-normalized one-dimensional pre-multiplied energy corresponding to the contour plots of figure 11 spectra are shown. The plots correspond to four wall-normal locations shown as white lines in figure 11 i.e. (*a*) $z^+ \approx 15$, (*b*) $z^+ \approx 45$, (*c*) $z^+ \approx \sqrt{15Re_\tau}$ and (*d*) $z^+ \approx 0.6Re_\tau$. Each plot shows the following profiles, PWJ HWA based $k_x\phi_{\widetilde{uu}}$ (——, red), PWJ PIV based streamwise spectra $k_x\phi_{uu}$ (——, blue), PWJ PIV based spanwise spectra $k_x\phi_{ww}$ (– – –) and matched ZPGBL HWA based $k_x\phi_{uu}$ of Nugroho *et al.* (2013) (——). The spatial location $\lambda \approx 2\delta$ (- - - - - -) is also highlighted.

over a range of $Re_\tau = 2740$–22884 that at the location of the inner peak $z^+ = 15$, the inner normalized, streamwise, small-scale, pre-multiplied spectrum distribution ($k_x^+\phi_{uu}^+$) is identical i.e. the small-scale contribution to the inner peak is invariant with Re_τ. Particularly at $z^+ = 15$ there is a peak in $k_x^+\phi_{uu}^+$ at $\lambda_x^+ \approx 1000$ which is invariant with Re_τ. Hence, based on the similarity in the near-wall production, it is reasonable to expect that the near-wall finer scales in a PWJ, would also have structures of inner-normalized scale with a peak comparable to $\lambda_x^+ \approx 1000$. Figure 12(*a*) compares the streamwise pre-multiplied spectra in the PWJ and the ZPGBL at $z^+ \approx 15$. There is a clear peak at $\lambda_x^+ \approx 1000$ in the spectra corresponding to the ZPGBL while the PWJ shows no clear peak in the smaller scales. This is due to the intrusion of the extremely energetic, outer larger scales into the near-wall region and/or insufficient scale separation at the local Reynolds number under consideration. Therefore, $\lambda_x = 2\delta$ ($\cdots\cdots$ in figure 12) is used as the discriminator to distinguish large scales from

https://doi.org/10.1017/jfm.2019.559 Published online by Cambridge University Press

the small scales while considering scale interactions in a subsequent section. The rationale being that this spectral location, i.e. $\lambda_x \approx 2\delta$, is sufficiently separated from $\lambda_x^+ \approx 1000$. This done with the proviso that some leakage between scales is inevitable, particularly as there is a peak in the larger scales at $\lambda_x = 2\delta$ when $z^+ \approx 15$.

There is more energy in the smaller scales than the larger ones in the near-wall region ($z^+ \approx 15$, figure 12*a*) in the case of the ZPGBL. At higher wall-normal locations the ZPGBL small-scale energy gradually decreases (figure 12*b–d*). Also at $z^+ \approx 15$, in the case of the ZPGBL, there is very little large-scale energy. In the case of the PWJ, as noted previously, there exists an energy peak at $\lambda_x \approx 2\delta$ at $z^+ \approx 15$. Away from the near-wall region, the peak in the PWJ spectra shifts to larger scales reaching a maximum of $\lambda_x \approx 6\delta$. The magnitude of this peak increases with increasing wall-normal distance and reaches a maximum at $z^+ \approx 0.6Re_\tau$. In the case of the PWJ, there is significant energy ($k_x^+\phi_{uu}^+ > 1$) in scales of streamwise extent $\lambda_x > 5\delta$ across the entire layer in contrast with the ZPGBL. Considering the smaller scales, away from the near-wall region, the PWJ has considerably higher inner-normalized small-scale energy across the entire layer when compared with the ZPGBL. This is anticipated as the increased energy in the large scales should lead to more energetic dissipative scales as indicated by the dissipation rate estimate in figure 9(*b*).

The spectra allow for the comparison of the PIV based spectra and the HWA based spectra. To the extent that the PIV based spectra are resolved, the agreement between the two is good. Notably, there appears to be a peak in $k_x^+\phi_{ww}^+$ at $\lambda_x^+ = 200 - 300$ which extends from the near-wall region up to $z^+ \approx \sqrt{15Re_\tau}$. At greater wall-normal locations the location of the peak in $k_x^+\phi_{ww}^+$ is not resolved by the current limited FOV. A similar near-wall peak in the wall-normal spectra has not been observed in a ZPGBL (Baidya 2016). It is also reasonable to conclude from figures 11 and 12 that Taylor's frozen hypothesis estimates reasonably the convective velocities of the smaller scales in the PWJ.

3.6. *Flow structures from flow visualization and instantaneous PIV snapshots*

The energy spectra clearly show the presence of extremely energetic, large-scale structures embedded within the PWJ. Past studies indicate broadly that these flow structures include flow eddies that are similar to those that occur within wall layers as well as free-shear layers (Katz *et al.* 1992; Dejoan & Leschziner 2005). Flow visualizations as well as instantaneous PIV realizations are now used to visualize some of the commonly seen instantaneous flow eddies.

Two flow visualization movies showing the evolution of flow structures within the PWJ are presented as supplementary material. Shown in figure 13 is a snapshot from one of the flow visualization movies. One of the movies shows the large-scale temporal evolution of the flow field while the other movie shows a portion of the same field with two zoomed-in views of the near-wall region, highlighting specific instantaneous flow structures. Here, nominal values of the relevant scales at $x/b = 137$ have been used to non-dimensionalize figure 13 and associated movies. Also shown are the nominal locations of the outer length scale δ and the location of the maximum velocity z_m at $x/b = 137$.

The movies show that the dominant flow structure is a large-scale motion with an anticlockwise rotation that has a large streamwise extent. This flow structure is associated with the outer free-shear layer and it spans the entire wall-normal extent of the PWJ. This large-scale structure is stretched in the streamwise direction by

https://doi.org/10.1017/jfm.2019.559 Published online by Cambridge University Press

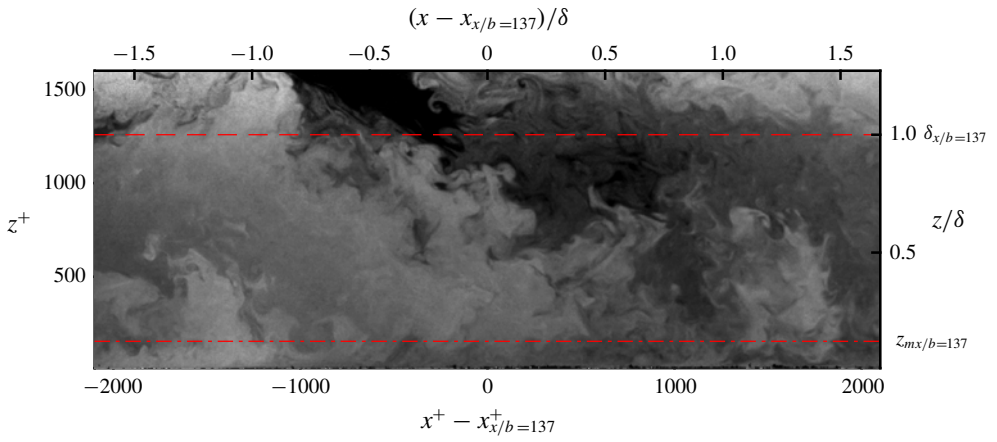


FIGURE 13. (Colour online) A snapshot of the flow visualized in the present facility that is part of a movie submitted as supplemental material. Nominal locations of the maximum velocity $z_{mx/b=137}$ (– – – –) and the outer length scale $\delta_{x/b=137}$ (– – –) at $x/b = 137$ are shown for reference.

the gradient caused due to the higher mean velocity around z_m. For the rest of this work we refer to this flow eddy as a type J (for jet) structure. The visualization and associated observation of the type J structures shown are exemplary of all the flow visualizations carried out i.e. this large-scale feature is ubiquitous to the PWJ. Such structures with large-scale rotation are also consistent with those observed in the DNS study of Naqavi *et al.* (2018).

Also seen in the movies, along with the type J flow eddies, are structures near the wall that are forward leaning or have a clockwise rotation. These are clearly observable in the movie showing a zoomed-in perspective of the near-wall region. An example of one such structure is highlighted in the supplemental video as a boundary-layer structure. This highlighted region shows two hairpin-vortex-like structures forming and possibly merging while convecting downstream. For the rest of this work we refer to these type of hierarchal flow eddies, typical of wall shear layers, as type W (for wall) flow structures.

Flow eddies of type W are unambiguously identified via instantaneous PIV vector fields. PIV vector fields highlighting flow eddies of type W, analogous to those seen in the near-wall region of canonical boundary layers are shown in figure 14. The colour contours in figure 14 indicate contours of swirl λ_{ci} (Christensen & Adrian 2001). A constant convection velocity of $U_c = (a)\ 0.75\ U_{mx/b=137}$ and $(b)\ 0.8\ U_{mx/b=137}$ have been used. The upward pointing arrows indicate vortices with clockwise rotation. Shown are two instances of vortex organization consistent with that of the hairpin vortex packet paradigm, similar to those seen for example in Christensen & Adrian (2001). The alignment angles of these packets (15° and 19° shown for reference in figures 14(*a*) and 14(*b*) respectively) are with respect to the vortices closest to the wall and are comparable to those reported for canonical wall layers. For example, Christensen & Adrian (2001) observed alignment angles of 16°–17° in a turbulent channel flow. However, the vortices that form part of the packet furthest from the wall appear to be at a higher inclination angle which may point to the influence of the outer layer structure on packets. Considering the vortex packet in figure 14(*b*) and

https://doi.org/10.1017/jfm.2019.559 Published online by Cambridge University Press

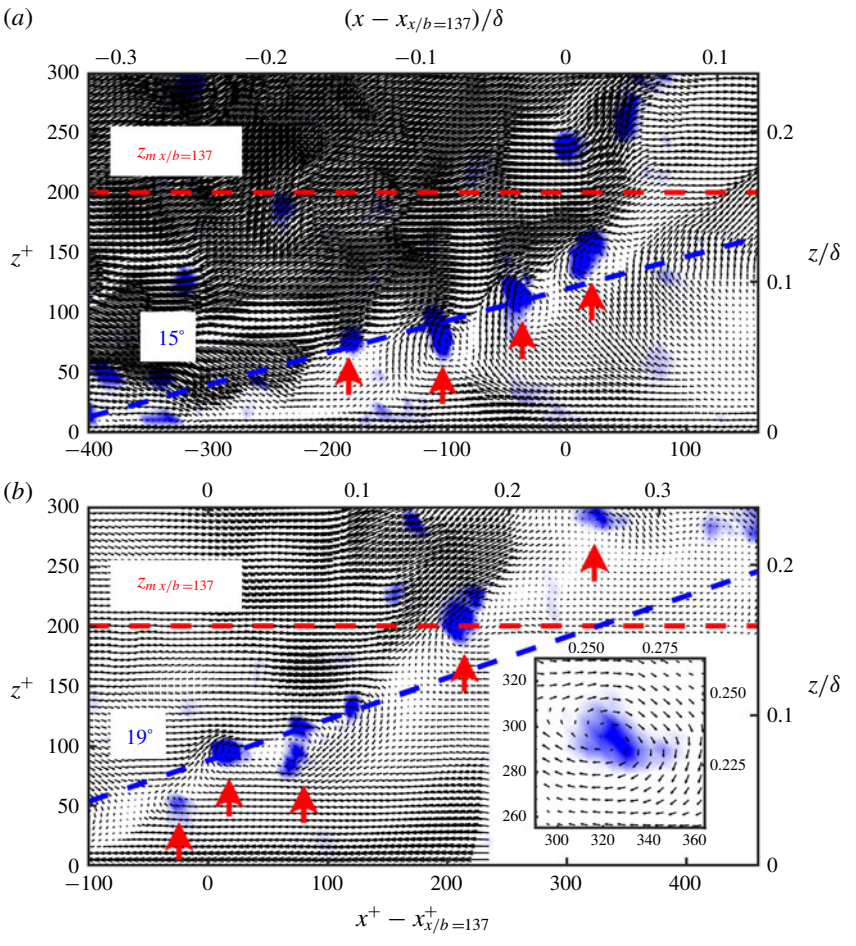


FIGURE 14. (Colour online) Two instantaneous velocity fields from the PIV measurements are shown. The vectors are overlaid on contours of constant swirl. A string of vortices with clockwise rotation which appearing to form a hairpin vortex packet are visualized in both vector fields. Convection velocities of (*a*) $U_{cl} = 0.75U_{mx/b=137}$ and (*b*) $U_{cl} = 0.8U_{mx/b=137}$ are used to aid in the visualization of the vortex centres. Upward pointing red arrows highlight vortices with clockwise rotation. The inset of (*b*) shows the upper most vortex of (*b*) with a convection velocity of $U_{cl} = 0.9U_{mx/b=137}$. A straight line (– – –, blue) approximately through the lower most vortex cores, at an angle of (*a*) 15° and (*b*) 19° are shown for reference. The line (– – –, red) indicates the nominal location of $z_{mx/b=137}$.

the supplemental flow visualization it is also clear that these type W eddies are seen to extend above z_m into the outer jet layer.

In the near-wall region ($z^+ < 400$), multiple instances of vortices with clockwise rotation, sometimes in the form of packets, were seen in nearly every instantaneous PIV realization. As seen in figure 14(*b*), it was also observed that not all vortices that appear to form a vortex packet were travelling at a constant convection velocity i.e. it was not always possible to visualize an ideal vortex structure in a single packet using a constant convection velocity. For example, the vortex structure of the topmost vortex

https://doi.org/10.1017/jfm.2019.559 Published online by Cambridge University Press

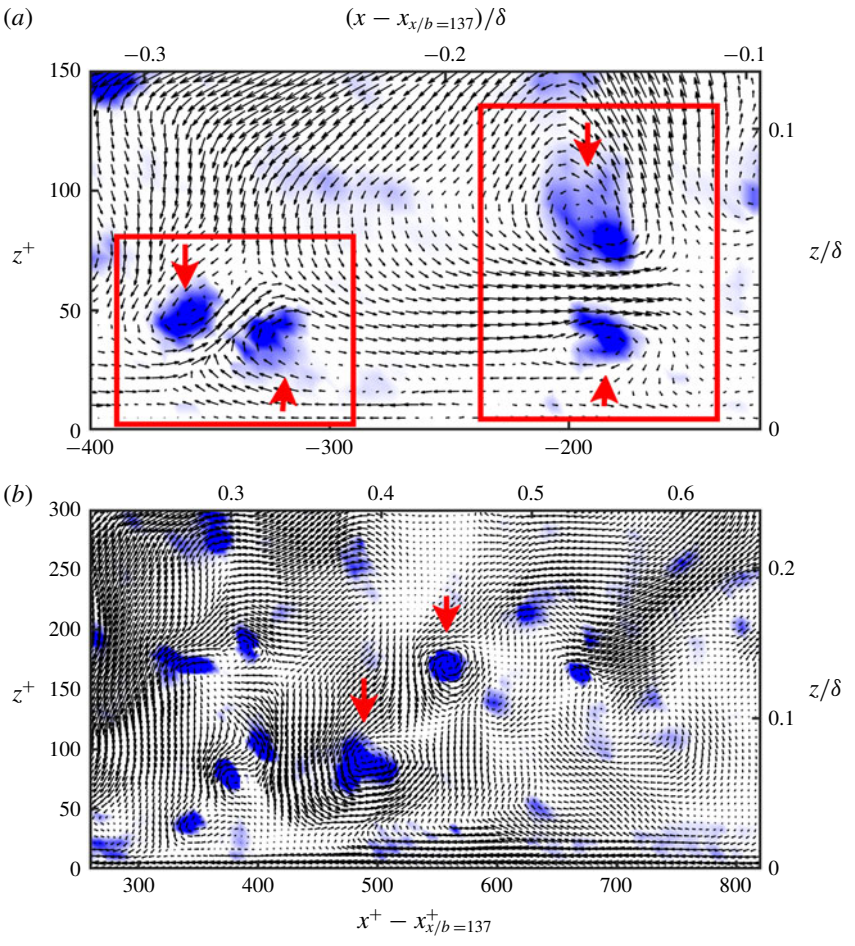


FIGURE 15. (Colour online) Two instantaneous velocity fields from the PIV measurements are presented. The vectors are overlaid over contours of constant swirl. Upward pointing red arrows highlight vortices with clockwise rotation while the downward pointing one indicates vortices with counter-clockwise rotation. In (*a*) Reynolds decomposition is used while in (*b*) a convection velocity of $U_{cl} = 0.75U_{mx/b=137}$ is used to aid in the visualization of the vortex centres In (*a*) the red rectangles highlight two counter-rotating, mushroom-like vortex pairs in the near-wall region while in (*b*) two instances of vortices with counter-clockwise rotation in the near-wall region are highlighted.

in figure 14(*b*) was better visualized using a convection velocity of $U_c = 0.9U_{mx/b=137}$ (shown in the inset of figure 14*b*).

Also seen less often, but consistently in both the flow visualizations as well as PIV realizations, were mushroom-like counter rotating vortex pairs. Two typical instances of such mushroom-like vortex pairs seen in the near-wall region have been highlighted in the supplemental flow visualization movie. Two exemplary instances from instantaneous PIV realizations are also shown in figure 15(*a*). Here, an upward pointing arrow indicates a clockwise rotating vortex while a downward pointing arrow indicates a counter-clockwise rotating vortex. Also observed often were several

https://doi.org/10.1017/jfm.2019.559 Published online by Cambridge University Press

isolated instances of counter-clockwise rotating vortices in the near-wall region as shown in figure 15(*b*) (a couple of them indicated by the downward pointing arrow).

3.7. *Large-scale features from two-point correlations*

The flow visualizations and instantaneous PIV realizations reveal at least two broad classes of large-scale flow structures, referred to as type J and type W, embedded within the PWJ. Two-point correlations are now used to provide a statistical estimate of the scale and orientations of these flow features. The two-point correlation at a reference streamwise location x_r and wall-normal location z_r is defined as

$$R_{ik}(\Delta x, z; x_r, z_r) = \frac{\overline{u_i(x_r + \Delta x, z_r) u_k(x_r + \Delta x, z)}}{\sigma_i(z_r)\sigma_k(z)}, \tag{3.8}$$

where u_i and u_k are the $\imath$th and kth velocity component respectively, Δx the streamwise spatial separation, z_r the reference wall-normal location, x_r is the reference streamwise location, $\sigma_i^2(z_r) = \overline{u_i^2(x_r + \Delta x, z_r)}$ and $\sigma_k^2(z) = \overline{u_k^2(x_r + \Delta x, z)}$. No streamwise averaging of the velocity field was carried out while evaluating equation (3.8). Two-point correlations were calculated at a single streamwise reference location nominally located at $x_r/b \approx 137$. Equation (3.8) is first evaluated from the velocity fields corresponding to each PIV image pair and subsequently ensemble averaged across all image pairs.

Shown in figure 16(*a*,*b*) are the contours of R_{uu} at $z_r^+ \approx 15$. Wall-normal axes in both linear (figure 16*a*) and log (figure 16*b*) scales are shown. The corresponding contours of R_{ww} (figure 16*c*,*d*) and R_{uw} (figure 16*e*,*f*) are also shown. Figure 17 shows the contours of R_{uu}, R_{ww} and R_{uw} when (i) $z_r^+ \approx 0.6\, Re_\tau$, (ii) $z_r^+ \approx \sqrt{15 Re_\tau}$ and (iii) $z_r^+ \approx 45$, corresponding to the wall-normal locations highlighted in the discussion on the spectra. One-dimensional slices of the correlation profiles in the streamwise direction, through the self-correlation peaks, i.e. $R_{uu}(\Delta x, z_r)$, $R_{ww}(\Delta x, z_r)$ and $R_{uw}(\Delta x, z_r)$, are shown in figure 18. The wall-normal profiles through the self-correlation peaks, i.e. $R_{uu}(0, z)$, $R_{ww}(0, z)$ and $R_{uw}(0, z)$, are shown in figure 19. In figure 20 profiles of $R_{uu}(0, z)$, $R_{ww}(0, z)$ and $R_{uw}(0, z)$ are also shown with the wall-normal axis in log scale.

At $z_r^+ \approx 15$, the prominent structure seen in the contours of R_{uu} is a flow structure that is forward leaning. This is consistent with structures seen in a ZPGBL with Reynolds number invariant inclination angles reported from 11° to 17° (Hutchins & Marušić 2007*a*; Marušić & Heuer 2007; Tutkun *et al.* 2009; Wu & Christensen 2010; Guala, Metzger & McKeon 2011; Hutchins *et al.* 2011; Sillero, Jiménez & Moser 2014). A line at an angle of 12° is shown in figure 16 for reference. This structure is associated with the packets of streamwise aligned hairpin vortices (type W structures) which in the framework of Townsend are 'attached eddies' (Townsend 1976). Consistent with this notion, their scale increases with distance from the wall, indicated by the contours of R_{uu} (figure 16*a*,*b*) (Townsend 1976; Adrian *et al.* 2000; Christensen & Adrian 2001; Adrian 2007). The contour level of 0.1 is used to estimate the spatial extent of structures. The streamwise spatial distance spanned by $R_{uu}(\Delta x, z_r) > 0.1$ is defined as Δx_{uu} while Δz_{uu} is the wall-normal distance spanned by $R_{uu}(0, z) > 0.1$ (in figures 18–20). Similarly, we define Δx_{ww} and Δz_{ww} based on the profiles of R_{ww}. At $z_r^+ \approx 15$, the streamwise extent $\Delta x_{uu} \approx 1.19\delta$ (see figure 18*a*) while the corresponding wall-normal extent is shorter at $\Delta z_{uu} \approx 0.31\delta$ (see figure 19*a*).

Considering contours of R_{uu} at $z_r^+ \approx 45$ and $\sqrt{15 Re_\tau}$ (both $< z_m$) the forward leaning flow features, indicative of type W structures, are still seen. With increasing wall-normal distance, their streamwise extent increases from $\Delta x_{uu} \approx 1.19\delta$ when $z_r^+ \approx 15$

https://doi.org/10.1017/jfm.2019.559 Published online by Cambridge University Press

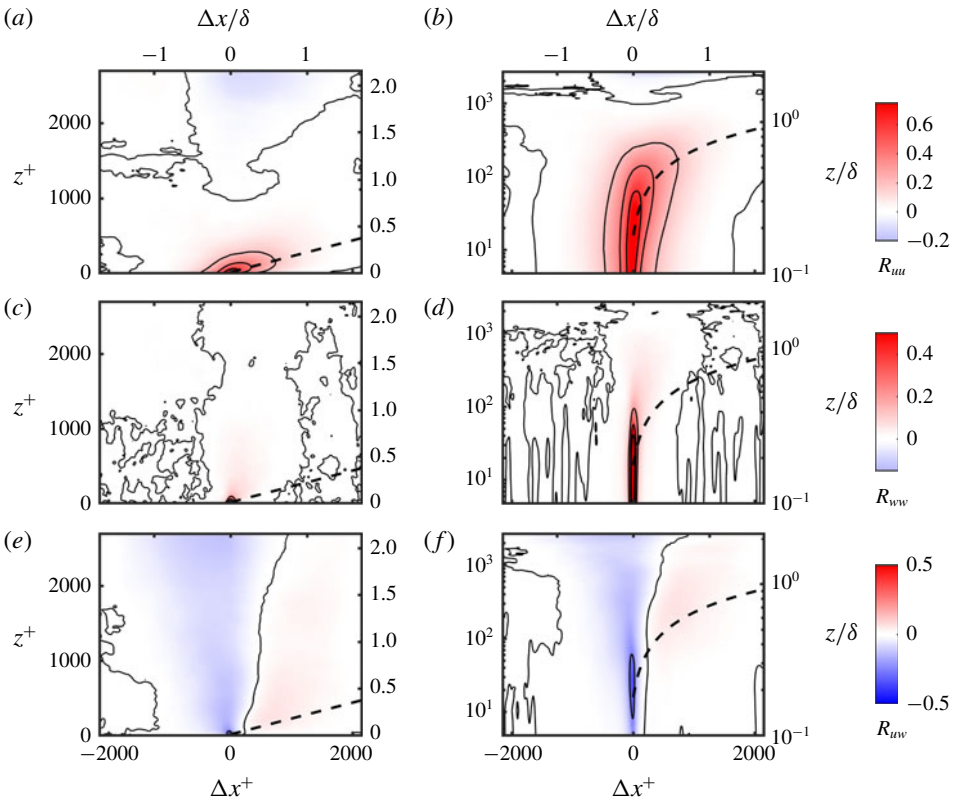


FIGURE 16. (Colour online) The contours of the two-point correlation when $z_r^+ \approx 15$ (*a*,*b*) R_{uu}, (*c*,*d*) R_{ww} and (*e*,*f*) R_{uw} are presented. The left column (*a*,*c*,*e*) shows the wall-normal ordinate in linear scale while the right column (*b*,*d*,*f*) shows the wall-normal ordinate in logarithmic scale. The solid lines represent the following contour levels – $R_{uu} \rightarrow [0, 0.2, 0.4, 0.6]$, $R_{ww} \rightarrow [-0.2, 0, 0.2, 0.4, 0.6]$ and $R_{uw} \rightarrow [-0.25, 0, 0.25]$. The line at 12° (– – –) is shown for reference indicating the nominal inclination angle for type W structures. It is noted that the scale of the vertical and horizontal axis are not equal.

to $\Delta x_{uu} \approx 1.45\delta$ when $z_r^+ \approx \sqrt{15Re_\tau}$ (see figure 18*a*). In the wall-normal direction the extent nearly doubles from $\Delta z_{uu} \approx 0.31\delta$ when $z_r^+ \approx 15$ to $\Delta z_{uu} \approx 0.61\delta$ when $z_r^+ \approx \sqrt{15Re_\tau}$. This is consistent with the hierarchal, attached-eddy type structures seen in canonical boundary layers (Tutkun *et al.* 2009). More significantly the signature of these wall type structures are seen to extend past $z_m \approx 0.165\delta$ well into the free-shear layer part of the flow at the three reference locations closest to the wall (i.e. $z_r^+ \approx 15$, 45 and $\sqrt{15Re_\tau}$).

At the outermost wall-normal location ($z_r^+ \approx 0.6Re_\tau$, see figure 17*a*), the contours of R_{uu} show the flow signature of structures that are backward leaning (with negative inclination angle) which are consistent with eddies of type J seen in the flow visualization. These structures J and W are also seen in the LES based two-point correlation maps of Banyassady & Piomelli (2014) in the PWJ development region ($x/b = 30$). The structures of type J are sheared by the high-momentum fluid beneath them, which is consistent with the flow visualization from the present work. This results in contours of R_{uu} that are tilted at a negative angle in the streamwise direction

https://doi.org/10.1017/jfm.2019.559 Published online by Cambridge University Press

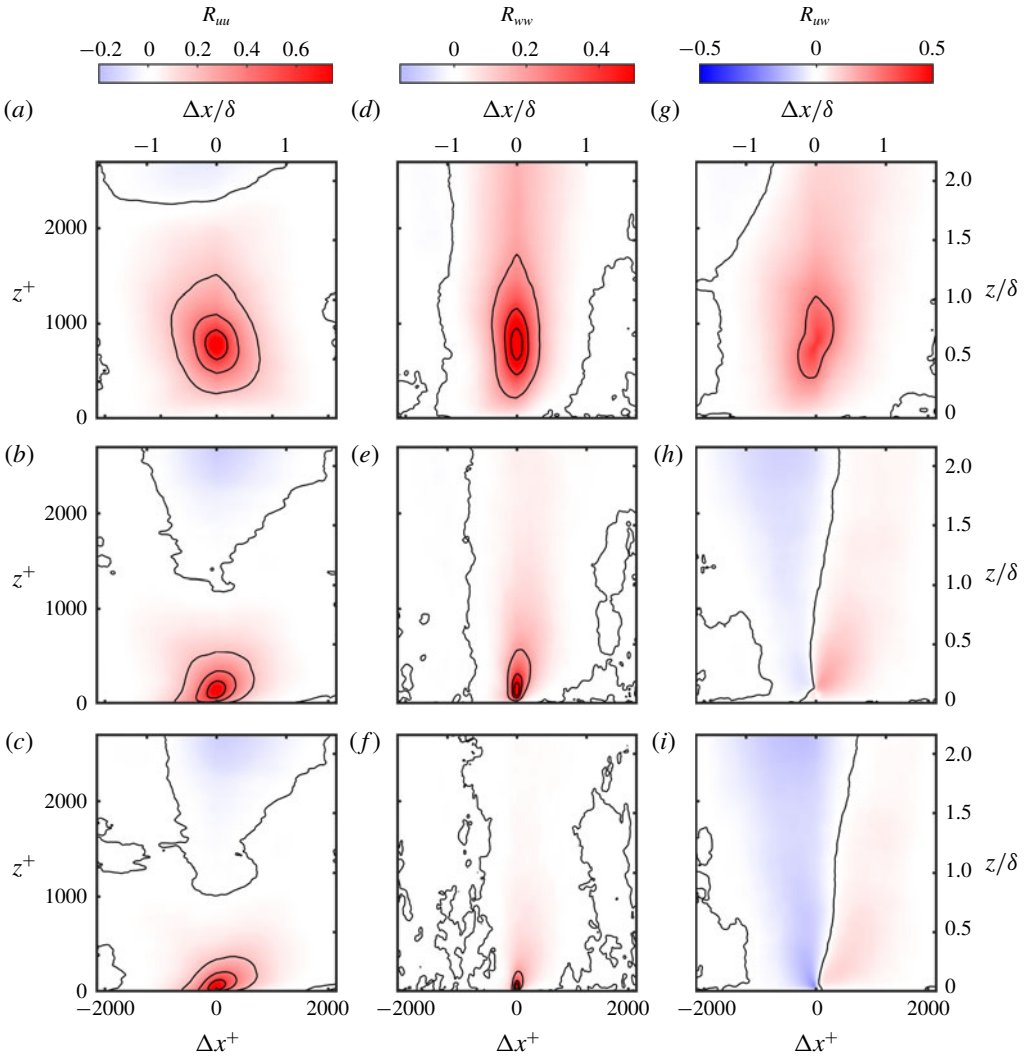


FIGURE 17. (Colour online) The contours of the two-point correlation (*a–c*) R_{uu}, (*d–f*) R_{ww} and (*g–i*) R_{uw} are presented. The top row (*a*,*d*,*g*) are the contours when $z_r^+ \approx 0.6Re_\tau$, the middle row (*b*,*e*,*h*) when $z_r^+ \approx \sqrt{15Re_\tau}$ and the bottom row (*c*,*f*,*i*) when $z_r^+ \approx 45$. The solid lines represent the contour levels identical to those in figure 16. It is noted that the scale of the vertical and horizontal axis are not equal.

(see figure 17*a*). The streamwise spatial extent is $\Delta x_{uu} \approx 1.73\delta$ when $z_r \approx 0.6Re_\tau$ while in the wall-normal direction $\Delta z_{uu} \approx 1.45\delta$, resulting in an aspect ratio of 1.19. It is again noted that the spatial signature indicative of type J structures intrudes into the wall layer i.e. below z_m (see figures 19*a* and 20*a*).

Considering the contours of R_{ww} a band of positively correlated wall-normal velocity is seen at all reference locations (see figures 16*c*,*d* and 17*d–f*). This is indicative of correlated motion towards or away from the wall. The reference locations in the wall region ($z_r < z_m$) are considered. In this region the streamwise spatial extent increases with wall-normal distance from $\Delta x_{ww} \approx 0.18\delta$ when $z_r^+ \approx 15$ to $\Delta x_{ww} \approx 0.98\delta$ when

https://doi.org/10.1017/jfm.2019.559 Published online by Cambridge University Press

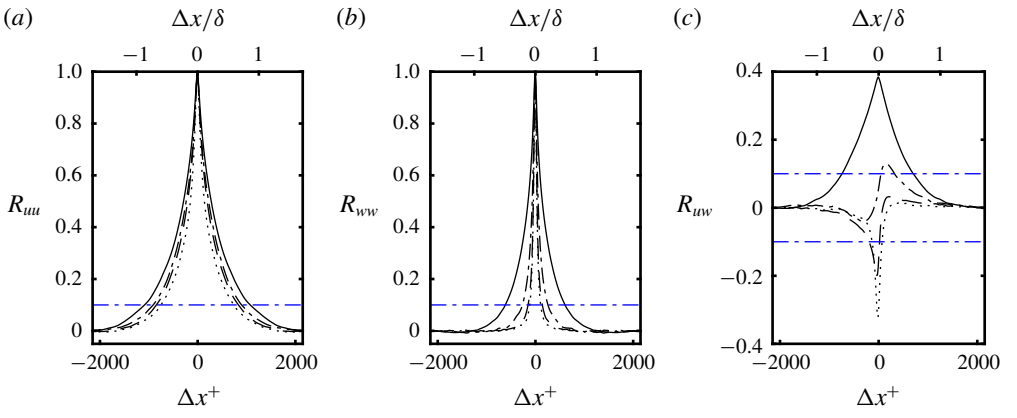


FIGURE 18. (Colour online) The streamwise profiles of the two-point correlation function through the self-correlation peak i.e. (*a*) $R_{uu}(\Delta x, z_r)$ (*b*) $R_{ww}(\Delta x, z_r)$ and (*c*) $R_{uw}(\Delta x, z_r)$ are presented. The lines correspond to the reference locations z_r are as follows: $z_r^+ \approx 15$ (- - - - - -), 45 (– – –), $\sqrt{15Re_\tau}$ (– – – – –) and $0.6Re_\tau$ (——).

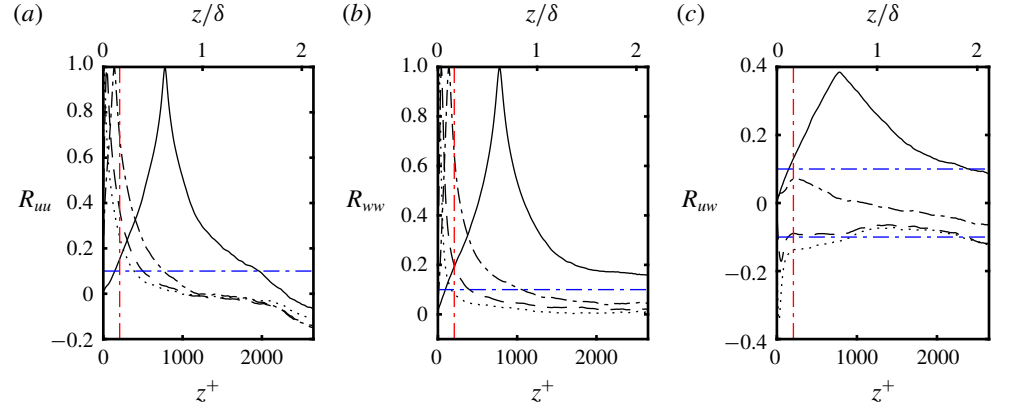


FIGURE 19. (Colour online) The wall-normal profiles of the two-point correlation function through the self-correlation peak i.e. (*a*) $R_{uu}(0, z)$ (*b*) $R_{ww}(0, z)$ and (*c*) $R_{uw}(0, z)$ are presented. The lines styles are identical to figure 18.

$z_r^+ \approx 0.6Re_\tau$ (see figure 18*b*). In the wall-normal direction the spatial extent increases from $\Delta z_{ww} \approx 0.14\delta$ when $z_r^+ \approx 15$ to $\Delta z_{ww} \approx 0.32\delta$ when $z_r^+ \approx 45$ (the two z_r that are closest to the wall, see figure 19*b*). At both these locations the correlation coefficient $R_{ww} > 0.1$ at the measurement point closest to the wall. When $z_r^+ \approx \sqrt{15Re_\tau}$ and $z^+ \approx 0.6Re_\tau$ the region with $R_{ww} > 0.1$ does not extend down to the wall but still extends below z_m (see figure 20*b*). When $z_r^+ \approx \sqrt{15Re_\tau}$, $\Delta z_{ww} \approx 0.84\delta$ while when $z_r^+ \approx 0.6Re_\tau$, Δz_{ww} is larger than the PIV FOV. It is again noted when $z_r^+ \approx 45$ and $\sqrt{15Re_\tau}$ the region that Δz_{ww} spans extends from less than z_m well into the outer free-shear layer. It is concluded that the structures indicated by the contours of R_{ww} are smaller in scale than those which have a signature in the contours of R_{uu}. The contours of R_{ww} also show a slight forward inclination in the near-wall region. In the wall region ($z_r < z_m$)

https://doi.org/10.1017/jfm.2019.559 Published online by Cambridge University Press

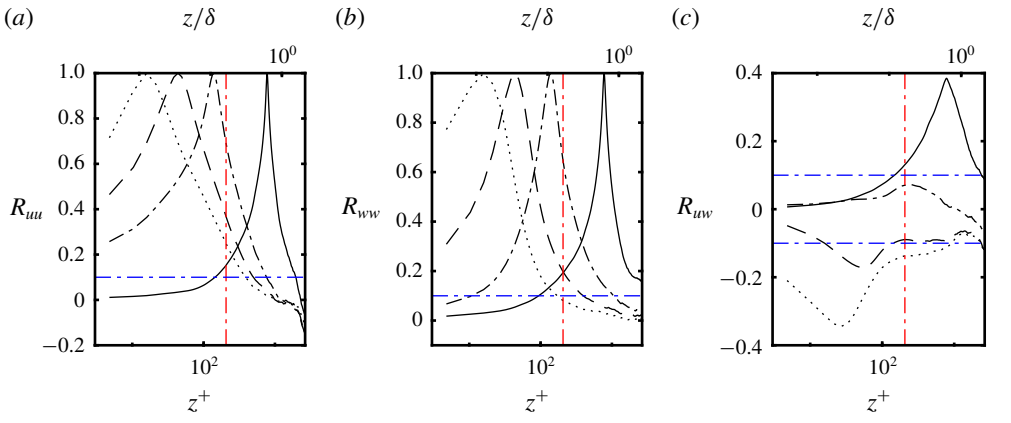


FIGURE 20. (Colour online) The wall-normal profiles of the two-point correlation function through the self-correlation peak i.e. (*a*) $R_{uu}(0, z)$ (*b*) $R_{ww}(0, z)$ and (*c*) $R_{uw}(0, z)$ are presented. The lines styles are identical to figure 18. This figure is identical to figure 19 except the wall-normal axis is in logarithmic scale.

the contours of R_{ww} and their extent are similar to those seen in a ZPGBL however, there are significant difference in the contours of R_{uw} (Volino, Schultz & Flack 2007).

Considering the contours of R_{uw} (see figures 16*e*,*f* and 17*g*–*i*), the contours corresponding to the reference locations in the wall region $z_r < z_m$ show a behaviour very different to those seen in canonical boundary layers. The contours of R_{uw} in canonical layers are backward leaning at roughly a 45° angle and are negatively correlated over the entire correlation domain (Volino *et al.* 2007). In canonical layers these are sweeps and ejections associated with hairpin vortex packets (Christensen 2001). In the case of the PWJ when $z_r^+ \approx 15$, 45 and $\sqrt{15Re_\tau}$ two forward leaning bands of oppositely correlated R_{uw} are seen. This type of correlation is consistent with vortical motion in the wall-normal–streamwise plane. However, when $z_r^+ \approx 45$ the contours of R_{uw} show a backwards lean at the contour levels below z_r (see bottom of figure 17*i*). This suggests that the signature of the forward leaning attached eddies exist in the correlation maps of R_{uw} but are overwhelmed by the signature of the more energetic J type structures.

The contours of R_{uu} are used to estimate the structure inclination angle β. Following Wu & Christensen (2010) β is calculated by first identifying the spatial location at each contour level that is farthest from the self-correlation peak. A straight line is then fitted through these points to yield β. Figure 21 shows contour lines of R_{uu} at the four wall-normal reference locations previously considered. Shown also are the points use as part of the linear fit used to calculated β. The darker contour line in figure 21 corresponds to the contour level 0.1 that was used to calculate Δx_{uu} and Δz_{uu}. The inclination angle β_w of the structure of type W was calculated to be $\beta_w = 12.78°$, 13.28° and 12.19° when $z_r^+ \approx 15$, 45 and $\sqrt{15Re_\tau}$ respectively. Hence, in this region β_w remains virtually unchanged. This agrees very well with the inclination angle of the structures associated with packets of hairpin vortices seen in canonical boundary layers (Tutkun *et al.* 2009). This is however counter to the observations from the current instantaneous PIV vector fields where the vortices furthest from the wall, that form a part of a hairpin vortex packet, appear to show a larger inclination angle.

The possible signatures of type J structures are also seen at the lower contour levels (top left corner of figure 21*a*,*b*) when $z_r^+ \approx 15$ and 45. This results in a stretched

https://doi.org/10.1017/jfm.2019.559 Published online by Cambridge University Press

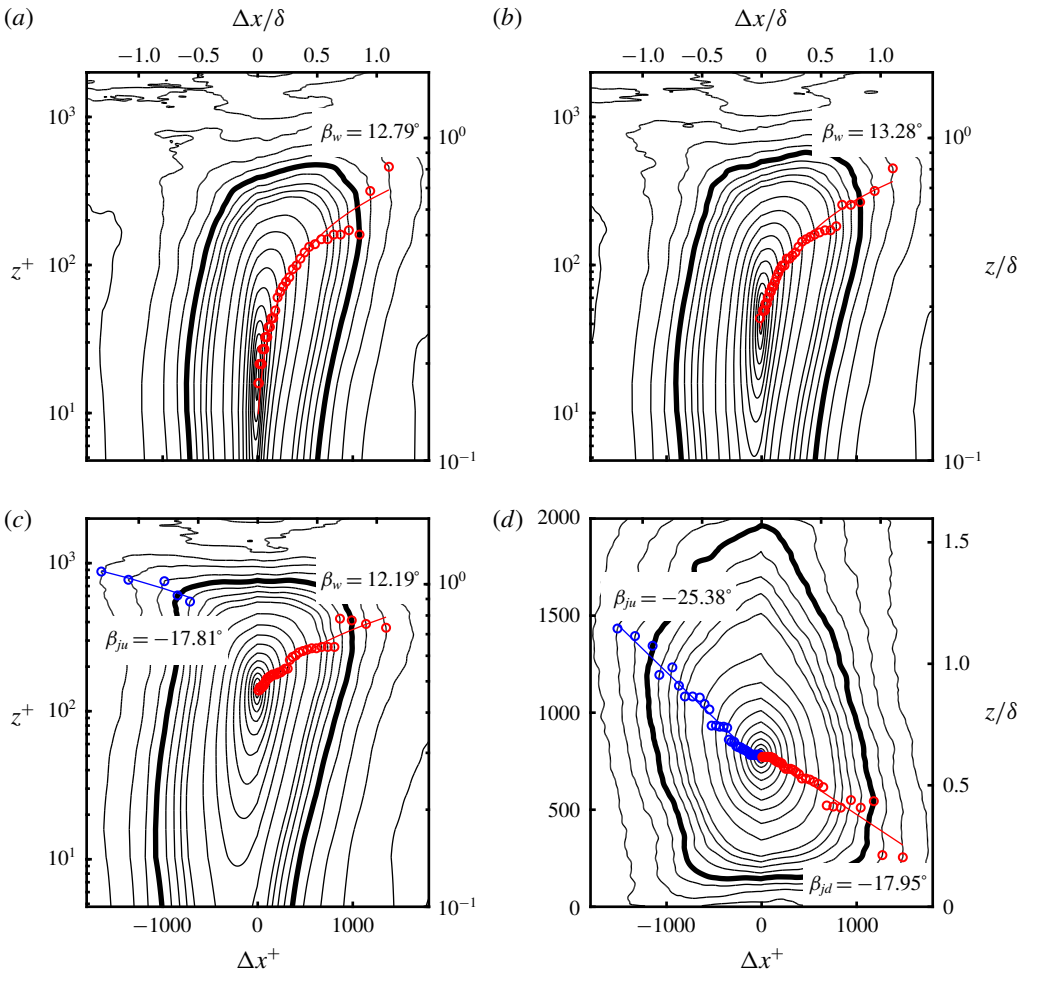


FIGURE 21. (Colour online) The contours of the two-point correlation R_{uu} when z_r^+ (*a*) $\approx$15, (*b*) $\approx$45, (*c*) $\approx\sqrt{15Re_\tau}$ and (*d*) $\approx 0.6Re_\tau$ are presented. The contour levels are $R_{uu} \rightarrow [-0.2, -0.175, \ldots, 0.2]$ for the lower contour levels and $R_{uu} \rightarrow [0.2, 0.275, \ldots, 0.95]$ for the higher contour levels. The darker contour line is the one corresponding to $R_{uu} = 0.1$. The symbols are the spatial locations which are the farthest from the self-correlation peak on a given contour level. It is noted that the scales of the vertical and horizontal axes are not equal.

contour map at the top left corner. At these reference locations, due to the limited number of contour levels at which the possible signature of type J structures are seen, we do not report an inclination angle for type J structures. However when $z_r^+ \approx \sqrt{15Re_\tau}$ the type J structure is seen to have an inclination angle $\beta_j = -17.81°$. This angle increases to a larger negative angle of $\beta_{ju} = -25.38°$ when $z_r^+ \approx 0.6Re_\tau$. These angles are the inclination angles that correspond to the upper contour levels i.e. contour levels when $z > z_r$, indicated by the subscript u. It is noted that at $z_r^+ \approx 0.6Re_\tau$, the lower contour levels show a stretching along the vertical. At these lower contour levels while evaluating β_{jd} the points that follow the inclination angles of the higher contour levels are used. The contour levels of $z < z_r$ are indicated

https://doi.org/10.1017/jfm.2019.559 Published online by Cambridge University Press

by the subscript d and the corresponding inclination angle was calculated to be $\beta_{jd} = -17.95°$. This difference in inclination angles when $z < z_r$ and $z > z_r$ is indicative of the stretching of the structure J by the higher-momentum fluid around z_m.

The two-point correlations show evidence of forward leaning structures (type J) in the near-wall region and larger structures (type W) in the outer jet region. As discussed, the contours of R_{uu} in figures 16(*a*,*b*) and 17(*b*,*c*) corresponding to the lower three z_r considered, appear to show the signature of the outer structure in the top left corner in the form of stretched contours. There are a few possibilities to consider. One is that the stretching of the contours are caused by the energetic outer J type structures intruding into the near-wall region. A similarly stretched contour of R_{uu} was reported by Sillero *et al.* (2014) in a turbulent channel flow ($Re_\tau = 2000$), albeit further away from the wall ($z_r/\delta = 0.8$). Hence, another possibility to consider is that this is a modification to the type W structures in response to the outer structures. This is similar to the stretching seen in the channel flow but it just is seen at lower wall-normal locations in the PWJ. In this context, the contours of R_{uu} are used to show that these are likely the intrusion of the outer layer structures into the near-wall region. It is also noted that the flow visualizations show that these outer structures reach the wall region ($z < z_m$) lending support to this viewpoint.

The structure inclination angles of the type W structures appear to be invariant around $\beta_w \approx 12°$–$14°$ in the near-wall region (when $z_r^+ < 150$) as noted before. However, when z_r^+ increases further, they were observed to start to decrease and gradually transition into the negative angle of the lower half ($z < z_r$) of the structure of type J i.e. the angle $\beta_{jd} = -17.85°$ (see figure 21*d*). Shown in figure 22 are the contours of R_{uu} when $z_r^+ = 315$. Also shown are the spatial locations at each contour level that is farthest from the self-correlation peak, which are the locations used to calculate β. These are shown for several reference locations i.e. $z_r^+ = 315,\ 350,\ 375$ and 400. These spatial locations are shown for points associated with the type W structures (points seen in the region $\Delta x > 0$). Also shown are those points possibly associated with type J structures (points seen in the top left corner). When considering the points associated with the type W structures, they show a positive inclination angle β at the higher contour levels. At the lower contour levels, these spatial locations are seen to jump to lower wall-normal locations resulting in an inclination angle that is close to zero. In other words when considering only the forward leaning contour levels (the higher contour levels), the inclination angle β is positive. When the outermost contour levels (lower contour levels) are considered they indicate a lower nearly zero β. On the other hand, at the top left corner the spatial locations associated with the structures of type J appear to result in a near constant inclination angle. If these two type of structures J and W co-exist within the PWJ, then when z_r is close to the wall we expect the type W structures to contribute to the higher contour levels while we would expect the outer, lower contour levels (those further away from the wall) to be primarily influenced by the more energetic outer scales. The jump we see in the inclination angle β is consistent with this viewpoint. At higher z_r than the ones presented in figure 22, the inclination angle in the region $\Delta x > 0$ converges to a single lower, more negative one. The inclination angle then starts to become more and more negative eventually leading to the large negative inclination angle β_{jd} seen in the lower half of figure 21(*d*) when $z_r^+ \approx 0.6Re_\tau$. Hence, this supports the view that the stretched contours of R_{uu} seen when z_r is close to the wall is the signature of the outer J structures intruding into the near-wall region. This would also explain the nearly invariant inclination angle β_w when $z_r < 150$ even

https://doi.org/10.1017/jfm.2019.559 Published online by Cambridge University Press

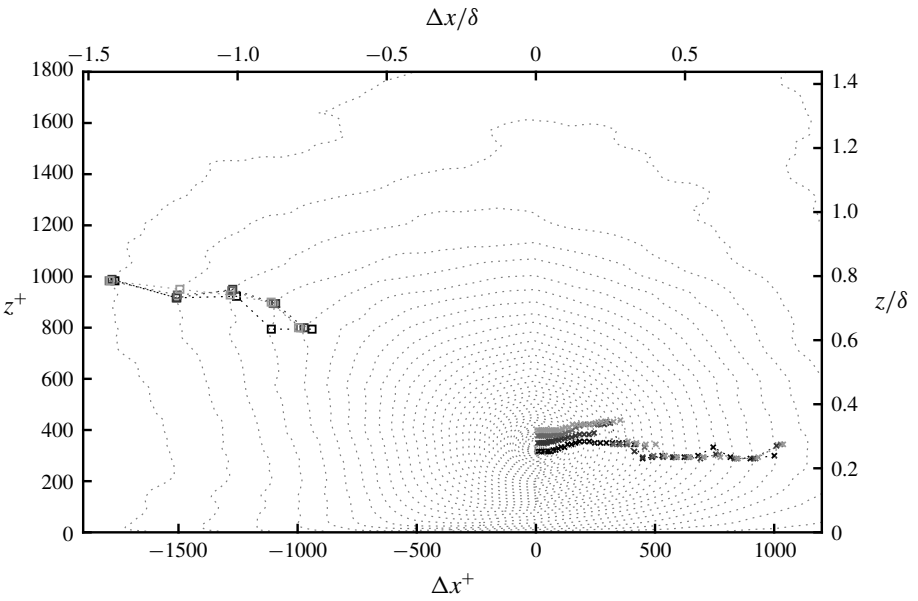


FIGURE 22. The contours of the two-point correlation R_{uu} when $z_r^+ \approx 350$. The symbols are the spatial locations which are the farthest from the self-correlation peak on a given contour level when $z_r^+ \approx 315$, 350, 375 and 400. The darker symbols correspond to the lower z_r^+. The spatial locations associated with both type W structures (points seen when $\Delta x > 0$ (×)) as well as type J structures (points in the top left corner (□)) are shown. It is noted that the scales of the vertical and horizontal axes are not equal.

though the instantaneous PIV vector fields seems to indicate that the vortices further away from the wall, that are part of hairpin packets, have higher inclination angles. In other words the effect of the intrusion of the outer structure J into the near-wall region is to contaminate the signature of type W structures as seen in the contours of R_{uu} in the wall region. This contamination reduces the inclination angle of type W structures, as calculated using contour levels, resulting in a near constant β_w in the wall region.

3.8. *Convection velocity and Taylor's frozen hypothesis*

Conditional averages of the PIV velocity field are now used to assess the applicability of Taylor's frozen hypothesis as well as the convection velocities of the large-scale structures in a PWJ. A conditionally averaged streamwise velocity field $\overline{u_c}(\Delta x, z)$ is defined as the spatial average conditioned on an event at a specific wall-normal location z_c. Chung & McKeon (2010) used conditional averages derived from LES velocity fields to estimate the large-scale features in a FDCF. They conditioned on large-scale, low-speed ($u < 0$) velocity events at several wall-normal locations to visualize average large-scale structures. Studies have also used an uncalibrated, near-wall hot-film in conjunction with a wall-normal hot-wire to visualize large-scale structures in a ZPGBL using conditionally averaged velocity fields (Hutchins *et al.* 2011; Talluru *et al.* 2014). Here, the condition used was a large-scale, low skin friction event ($\tau_w < 0$). Following these studies, we use conditional averages conditioned on low-speed, fluctuating streamwise velocity events i.e. $u(x, z_c) < 0$, to

https://doi.org/10.1017/jfm.2019.559 Published online by Cambridge University Press

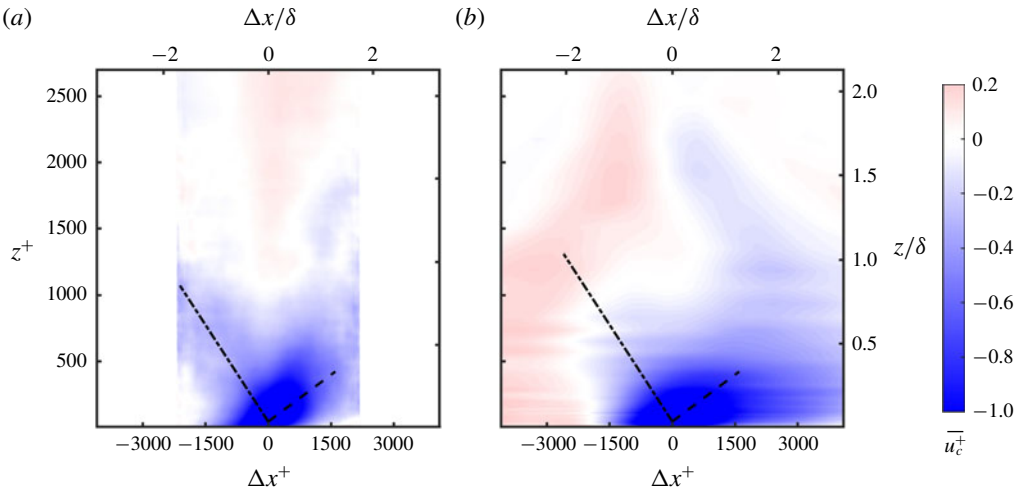


FIGURE 23. (Colour online) (*a*) Colour contours of the inner-normalized conditional streamwise velocity field $\overline{u_c^+}$ based on PIV measurements when $z_c^+ \approx 45$. (*b*) Shown are the colour contours of the inner-normalized conditional effective velocity field $\widetilde{u_c^2}$ based on combined hot-film/hot-wire measurements calculated using Taylor's frozen hypothesis. The straight lines highlighting inclination angles of structures of type J (– – – – –) and W (– – –) are shown for reference.

visualize the large-scale features of the PWJ. Qualitatively the structures captured by the low-speed conditional fields are similar to those flow features captured by two-point correlations. The conditional fields are presented here to make appropriate comparisons with combined wall hot-film/hot-wire measurements. While calculating the conditional fields the average was carried out over the entire spanwise extent of the FOV i.e. the spreading of the jet over the FOV was ignored.

Conditional fields of the streamwise effective velocity $\widetilde{u}_c$ are also calculated from the combined wall hot-film and HWA based measurements. Here, the conditional fields are conditioned on a low-speed, fluctuating, wall shear stress event i.e. when the fluctuating uncalibrated hot-film signal $V_{hf} < 0$. The hot-film signal was low-pass filtered, using $\lambda_x = 2\delta$ as the scale separator, to avoid conditioning on small-scale events. The contours of the conditional field $\widetilde{u}_c(\Delta x, z)$ is shown in figure 23(*b*). Here Taylor's frozen hypothesis, using the local mean velocity as the convection velocity, was again used to convert a temporal signal to a spatial one. The low-speed structure visualized is centred around a low-speed fluctuating velocity event at $z_c^+ \approx 45$. This structure again is forward leaning and is consistent with the type W structures seen in the contours of R_{uu}. They are also consistent with conditional structures visualized in a ZPGBL using combined hot-film HWA measurements (Hutchins *et al.* 2011; Talluru *et al.* 2014). A conditional field $\overline{u_c}$ as calculated from the PIV measurements conditioned on $u(x, z_c^+ \approx 45) < 0$ is shown in figure 23(*a*) for comparison. Seen again is a forward leaning structure indicative of type W structures. Comparing figure 23(*a*,*b*) it is seen that the forward leaning structure (type W) from the hot-wire/hot-film measurements is stretched in the streamwise direction when compared with those from the PIV based measurements. This indicates that Taylor's frozen hypothesis over estimates the convection velocities of the type W structures. It is thus noted that at least for the large-scale structures of type W the spatial scales estimated

https://doi.org/10.1017/jfm.2019.559 Published online by Cambridge University Press

by the hot-wire based energy spectra (figures 11 and 12) are overestimated by the use of Taylor's frozen hypothesis. This is in contrast with the finer scales whose convection velocity appears to be estimated reasonably well by using Taylor's frozen hypothesis, as seen when compared with the spectra calculated using the PIV based measurements. Considering type J structures, their signature is barely visualized in the conditional plot calculated from the hot-wire/hot-film measurements (figure 23). The outer layer structures were shown to have a spectral peak at $\lambda_x \approx 6\delta$ using Taylor's frozen hypothesis (see figure 12). This is significantly lower than their extent $\Delta x_{uu} \approx 1.73\delta$ estimated using two-point correlations. It thus appears that Taylor's frozen hypothesis also overestimates the convection velocity of type J structures.

3.9. *Scale interactions*

Several studies have shown an interaction between the large scales and the finer scales of the flow in wall-bounded turbulence (Mathis *et al.* 2011*b*; Duvvuri & McKeon 2015). Mathis *et al.* (2009*a*) used an amplitude modulation coefficient to characterize this modulation effect which is defined as

$$R_{AM} = \frac{\overline{u_L\ E_L(u_s)}}{\sqrt{\overline{u_L^2}}\sqrt{\overline{E_L(u_s)^2}}}. \tag{3.9}$$

Here, u_L is the large-scale component of the streamwise velocity fluctuations and $E_L(u_s)$ is the filtered large-scale envelope of the streamwise small-scale fluctuations. The large-scale velocity component u_L is identified by using Taylor's frozen hypothesis and the envelope of the small-scale fluctuations $E_L(u_s)$ is then obtained by applying a Hilbert Transformation to the small-scale component u_s. The large-scale component of this envelope is then extracted by using an appropriate filter. In the present case the effective velocity as measured by HWA is used to calculate R_{AM}. The large-scale component of the local effective velocity is used to estimate u_L following several past studies that have used and assessed this approach (Mathis *et al.* 2009*b*; Schlatter & Orlu 2010; Jacobi & McKeon 2013; Pathikonda & Christensen 2017). This is justified as the spectra of figure 11 as well as the two-point correlations show the penetration of the outer large-scale structures into the wall region.

As discussed in a preceding section, a threshold of $\lambda_x = 2\delta$ is used to separate the larger scales from the finer scales with the proviso that some leakage between scales is inevitable. Figure 24(*a*) shows the total inner-scaled effective streamwise turbulent intensity. This turbulent intensity is then decomposed into its small-scale and large-scale components and also shown in figure 24. The small-scale intensity has a peak near $z^+ \approx 15$ which is the inner peak associated with the near-wall turbulent cycle. Further away from the wall the small-scale intensity drops and reaches a smaller peak in the outer jet region $z/\delta \approx 0.6$. It is likely that this small-scale intensity has leakage from larger scales due to insufficient scale separation. The large-scale intensity initially increases sharply in the near-wall region and then gradually reaches a peak around $z/\delta \approx 0.7$.

The amplitude modulation coefficient R_{AM} through the layer is shown in figure 24(*b*). There is a positive correlation between the large scales and the envelope of the small scales across the entire layer indicating a strong degree of amplitude modulation. Shown also in figure 24(*b*) is R_{AM} corresponding to the matched ZPGBL measurements of Nugroho *et al.* (2013) where again a discriminator of $\lambda_x = 2\delta$ was used to separate the large scales from the small scales. In the near-wall region R_{AM}

https://doi.org/10.1017/jfm.2019.559 Published online by Cambridge University Press

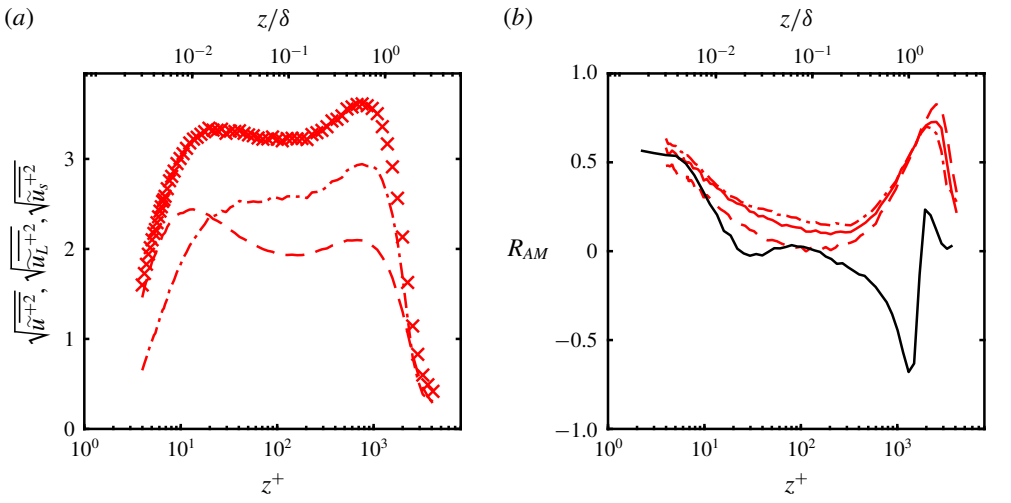


FIGURE 24. (Colour online) (*a*) The inner-normalized effective turbulent intensity profile of the PWJ showing total (×) as well as small-scale (– – –) and large-scale components (– – – – –). (*b*) The amplitude modulation coefficient R_{AM} of the PWJ when the discriminator used to separate the large scales from the small scales is $\lambda_x = \delta$ (– – – –), $\lambda_x = 2\delta$ (——, red) and $\lambda_x = 4\delta$ (– – –) is shown. Also shown is R_{AM} of the matched ZPGBL of Nugroho *et al.* (2013) (——) when the discriminator is $\lambda_x = 2\delta$.

are nearly identical when comparing the PWJ and the ZPGBL. Chung & McKeon (2010) point out that R_{AM} can be interpreted as a phase difference between flow scales. Hence considering inner–outer interactions, the near-wall region of R_{AM} is the only true indication of the inner–outer interactions in the flow with R_{AM} away from the wall being an artefact of the relative arrangement of low-speed and high-speed structures within the PWJ (Pathikonda & Christensen 2017).

Two other thresholds of $\lambda_x = \delta$ and $\lambda_x = 4\delta$ were also used to discriminate the large scales from the finer scales. These were considered to assess the robustness of this modulating effect. It is seen that the profiles of R_{AM} when the discriminator is $\lambda_x = \delta$ is nearly identical to that when $\lambda_x = 2\delta$. This suggests that scales with $\delta < \lambda_x < 2\delta$ have a minimal influence on the modulating effect. However when a scale discriminator of $\lambda_x = 4\delta$ is used, in the near-wall region and past $z_m^+ \approx 200$ the profile of R_{AM} is lower than that when $\lambda_x = 2\delta$. Figure 12 indicates that the outer jet layer structures (type J) have a spatial signature of $\lambda_x \approx 6\delta$, based on Taylor's frozen hypothesis. Hence, we also conclude that these outer layer structures indeed do contribute to the modulation of the finer scales in the wall region. It is again noted here that the spatial signature of type W structures are overestimated by the use of Taylor's frozen hypothesis.

4. Discussion

The flow visualization, the instantaneous PIV vector fields and the two-point correlations collectively present evidence for at least two large-scale features embedded within the PWJ. One type of structure is the structure of type J with counter-clockwise large-scale rotation seen in the outer jet region of the PWJ with a footprint that appears to extend into the wall region ($z < z_m$). This is inferred from the contours of R_{uu} (figures 17–21). The prominence and the energy carried by these

https://doi.org/10.1017/jfm.2019.559 Published online by Cambridge University Press

outer structures (as indicated in the energy spectra) suggest some level of coherence in the spanwise direction.

The other structure is the structure of type W which is forward leaning and is consistent with the hairpin vortex packet paradigm. These are hierarchal structures that are attached to the wall. A different perspective interprets these structures as disorganized clusters of vortices (Jiménez 2012). These vortex clusters are associated in an average sense with a sweep and an ejection pair, a large velocity streak segment or roller with disorganized vorticity (Jiménez 2012). Despite the varying perspectives these type W structures are clearly attached eddies as the significant contour levels of the two-point correlation i.e. $R_{uu} > 0.1$ extend into the near-wall region ($z^+ < 20$). These inner boundary-layer like structures also intrude out into the jet region ($z > z_m$). Hence, there is an overlap region as hypothesized by George *et al.* (2000) in which both the outer J type structures and inner W type structures are interacting. It is also noted that the structures of type W are the LSM seen in canonical boundary layers.

With respect to the wall the outer J type may be considered detached in that the significant contour levels of the two-point correlation i.e. $R_{uu} > 0.1$ do not extend into the near-wall region ($z^+ < 20$). However, these structures are influenced by the wall. The contours of R_{uu} when $z_r \approx 0.6Re_\tau$ in figure 21(*d*) show a clear flattening of the lower contour levels, closer to the wall. This suggests that the motion of these structures are restricted by the presence of the wall which results in their inviscid 'splatting' onto the wall (Perot & Moin 1995; Dejoan & Leschziner 2006). The contours of R_{uw} (figure 17*h*,*i*) also suggest that these vortical structures are responsible for the turbulent transport between the two production peaks of the PWJ.

An aspect of the PWJ that has not been discussed due to the current observations being based on hot-wire and PIV measurements (in the streamwise-wall–normal plane) is the high spanwise turbulent intensities observed in the PWJ, particularly in the outer jet region (Abrahamsson *et al.* 1994). Hence, there are likely other structures (other than the type J and type W structures) that are also present within the PWJ, that perhaps measurements in the spanwise–wall-normal plane would reveal. One possibility for a structure is to consider the PWJ not only as a boundary layer and a shear layer but also as a mixing layer, due to the two differently scaled sources of turbulence encapsulated within it. In this context, the presence of structures similar to braid-like eddies seen in mixing layers (Browand 1986; Loucks & Wallace 2012) is a possibility.

Various aspects of the PWJ have some similarities to other wall-bounded flows despite key differences. The outer turbulent production peak observed is similar to that seen in adverse-pressure-gradient boundary layers (APGBL) where an outer peak in P^+z^+ (and streamwise turbulent intensity) was also noticed at a fairly moderate $Re_\tau = 3200$. This peak was attributed to inactive outer layer structures (Harun *et al.* 2013). However in contrast with the PWJ the mean viscous shear in the APGBL outer region is of opposite sign to that of the jet region in the PWJ. Another class of boundary layers with a large outer peak in the streamwise turbulent intensity, at moderate Re_τ, are those developing under the influence of large-scale free stream turbulence (FST) (Sharp, Neuscamman & Warhaft 2009; Dogan, Hanson & Ganapathisubramani 2016; Hearst, Dogan & Ganapathisubramani 2018). These flow fields also have large-scale intrusions from the outer FST into the near-wall region. The magnitude of this outer peak was seen to become comparable in magnitude to the inner peak at sufficiently large FST. However, the mean viscous shear in the case of the boundary layer under the influence of FST is also of opposite sign when compared to the outer region of the PWJ. What appears to be universal to the APGBL, the boundary layer under the effect

https://doi.org/10.1017/jfm.2019.559 Published online by Cambridge University Press

of FST as well as the PWJ is the robustness of the inner turbulence peak irrespective of the specific nature of the outer larger scales. This is despite the fact that all three flows show scale interactions between the larger scales (presumably from different origins) and the finer scales.

5. Conclusions

Detailed hot-wire anemometry and particle image velocimetry based measurements were carried out in a plane wall jet, developing in still air, at streamwise distances up to $162b$ (b is the PWJ exit slot width). Combined hot-wire and hot-film based measurements were also carried out at a streamwise location of $137b$. Comparisons with a zero-pressure-gradient boundary layer at nominally matched friction Reynolds number Re_τ were carried out were appropriate. The major observations and conclusions are summarized below.

(i) The plane wall jet has extremely energetic flow structures in the outer region when compared to the zero-pressure-gradient boundary layer at matched Reynolds number Re_τ. These structures appeared as energetic peaks in the streamwise and wall-normal turbulent intensity profiles as well as in the Reynolds shear stress profile.

(ii) The observed peak in the streamwise turbulent intensity was consistent with previously reported dependence on jet exit Reynolds number Re_j. In addition the dependence of the peaks in the wall-normal intensity and Reynolds shear stresses on Re_j was shown.

(iii) Contrary to the Reynolds shear stress τ_{uw} profiles observed in a zero-pressure-gradient boundary layer, τ_{uw} switches sign concomitant with a change in sign of the viscous shear stress profiles τ_{visc}. This leads to a region of very low turbulent production in the PWJ. There is a peak in the turbulent production in the near-wall region of the PWJ nearly identical in magnitude to that of the zero-pressure-gradient boundary layer. However, there is a larger production peak in the outer region with the region of low production lying between these two peaks. The estimated dissipation rate increases through the PWJ reaching a maximum also in the outer region.

(iv) The ratio of the production to dissipation rate showed that between the two production peaks the PWJ is not in equilibrium. This suggests that the turbulent energy is transported to this zone from the regions containing the two production peaks.

(v) The one-dimensional energy spectra show that these extremely energetic outer scales are primarily scales larger than the outer scale δ or large scales of motion. They extend across the entire PWJ layer and showed a peak in the spectra at $\lambda_x \approx 6\delta$ across most of the layer. Here, λ_x is the streamwise wavelength based on Taylor's frozen hypothesis.

(vi) Flow visualizations indicate that the prominent and most energetic flow feature seen is a large-scale vortical motion similar to the structures seen in free-shear layers. These are referred to as type J (for jet) structures.

(vii) Two-pointcorrelations also reveal a forward leaning large-scale flow structure in the wall region consistent with the signature of hairpin vortex packets. These are called type W (for wall) structures. Flow visualization and instantaneous particle image velocimetry vector fields reveal the presence of these hairpin vortex packets in the wall region ($z < z_m$).

https://doi.org/10.1017/jfm.2019.559 Published online by Cambridge University Press

(viii) The type J structures were observed to extend into the wall region and *vice versa* for the type W structures.

(ix) Comparison of the PIV based conditional plots with the hot-wire/hot-film based ones suggests that Taylor's frozen hypothesis overestimates the convection velocity of type W structures. Comparing the extents calculated from two-point correlations and those estimated from Taylor's frozen hypothesis it appears that Taylor's frozen hypothesis also overestimates the convection velocity of type J structures.

(x) Finally, it is shown that the large scales of the flow modulate the amplitude of the finer scales, indicative of an interacting flow.

Acknowledgements

The authors would like to gratefully acknowledge Nugroho *et al.* (2013) and Sillero *et al.* (2013) for making available the ZPGBL data. The authors would like to thank the anonymous reviewers for their insightful comments and the time expended. The authors would also like to gratefully acknowledge the U.S. Air Force Office of Scientific Research for support of this work through grant FA9550-16-1-0194 managed by Dr G. Abate.

Supplementary movies

Supplementary movies are available at https://doi.org/10.1017/jfm.2019.559.

Appendix A. Measurement of the friction velocity u_τ

The measurement of the mean wall shear stress τ_w in wall-bounded flows and subsequently the friction velocity u_τ has been historically challenging. In a PWJ, various techniques including Preston tubes, near-wall fits (linear or otherwise), correlations, etc. have been used to measure τ_w (refer to table 2 for relevant references). Here a near-wall fit based technique was used to measure the friction velocity.

Studies have pointed out the apparent universality of the inner-scaled near-wall ($z^+ < 10$) mean velocity profile in a PWJ when compared with other canonical wall-bounded flows (George *et al.* 2000; Tachie *et al.* 2002). George *et al.* (2000) point out that the Taylor's series expansion about $z^+ = 0$ gives rise to the linear velocity profile ($U^+ = z^+$) in the very-near-wall region ($z^+ \lesssim 3$) with the first non-zero term being the fourth power z^{+4}. Combining the near-wall Taylor's series expansion and a power law based on the asymptotic invariance principle they propose a composite velocity profile extending out to the overlap region of the PWJ of the following form:

$$\begin{aligned} U^+ \;=\; & (z^+ + c_4 z^{+4} + c_5 z^{+5}) \exp(-d z^{+6}) \\ & + C_i z^{+\gamma}(1 + \gamma a^+ z^{+-1} + \tfrac{1}{2}\gamma(\gamma-1)a^{+2} z^{+-2})(1 - \exp(-d z^{+6})), \end{aligned} \tag{A 1}$$

here $c_4 = -.0003$ and $c_5 = 1.35 \times 10^{-5}$ are constants governing the near-wall mean velocity profile. C_i and γ are Reynolds number $R_m = z_m U_m/\nu$ dependent constants which are determined by interpolation based on the parameters calculated by George *et al.* (2000). The damping parameter $d = 8 \times 10^{-8}$ blends the inner Taylor's series expansion with the overlap region power law, while $a^+ = -16$ is treated as a constant.

https://doi.org/10.1017/jfm.2019.559 Published online by Cambridge University Press

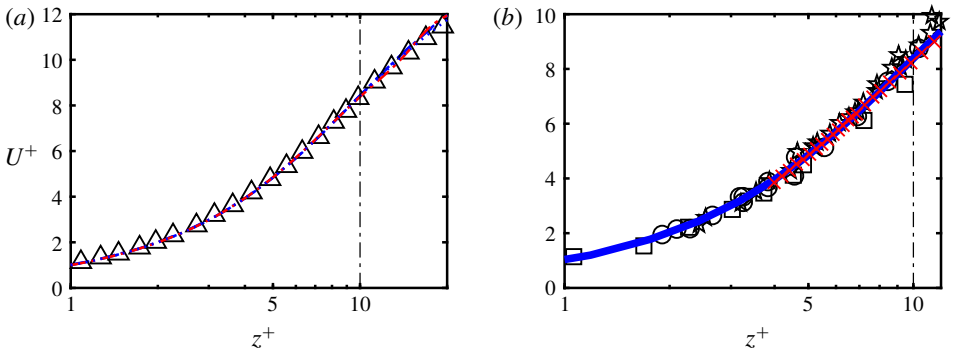


FIGURE 25. (Colour online) (*a*) The composite profile of George *et al.* (2000) (– – – –, red) is compared with the ZPGBL composite profile of Chauhan *et al.* (2009) (· · · · · ·), ZPGBL DNS of Sillero *et al.* (2013) at $Re_\tau = 1307$ (– – – –, blue), channel flow DNS of Lee & Moser (2015) at $Re_\tau = 2000$ (– – –) and the PWJ DNS of Ahlman *et al.* (2007) at $Re_j = 2000$ (△) (*b*) The curve fit used is compared with near-wall measurements in a PWJ from several sources (refer to table 2 for symbols) as well as an exemplary current measurement (×). The vertical line (– – – –) in both plots is the line $z^+ = 10$.

George *et al.* (2000) compared this composite profile (A 1) with measurements from a PWJ and a ZPGBL with good agreement. Tachie *et al.* (2002) have also shown using LDV measurements this universality of the near-wall inner-scaled mean velocity profile. Considering a ZPGBL, Chauhan *et al.* (2009) used a similar composite velocity profile to assess ZPGBL measurement quality. This composite profile has been shown to have excellent agreement with experimental data up to Reynolds numbers $Re_\tau = 22884$ (Kulandaivelu 2011).

Shown in figure 25(*a*) are the velocity distributions in the near-wall region $z^+ < 20$ as calculated using the composite profiles of George *et al.* (2000) and Chauhan *et al.* (2009). Also shown are the distributions corresponding to the ZPGBL DNS of Sillero *et al.* (2013) at $Re_\tau = 1307$, channel flow DNS of Lee & Moser (2015) at $Re_\tau = 2000$ and the PWJ DNS of Ahlman *et al.* (2007). The data of Sillero *et al.* (2013) and Lee & Moser (2015) have been obtained from the respective web-based databases while the data of Ahlman *et al.* (2007) have been digitized. The agreement between the various profiles is excellent with the profiles being virtually identical up to a wall-normal distance of $z^+ = 10$.

This universality of the inner-scaled near-wall mean velocity profile is used to measure the friction velocity through a least squares curve fit. Careful velocity measurements using a hot-wire anemometer were carried out in the near-wall region ($4 \leqslant z^+ \leqslant 10$) with fine wall-normal increments. At least 17 wall-normal locations lying between $4 \leqslant z^+ \leqslant 10$ were used (streamwise locations $x/b > 50$) while, locations below $z^+ < 4$ were discarded due to possible contamination from conduction to the wall (Hutchins & Choi 2002). The velocity profiles of figure 25(*a*) were collectively fitted with a fifth-order polynomial which was then used to fit the current measurements yielding a measure of u_τ. The least squares fit was also used to get an accurate measure of the wall ($z^+ = 0$) location. In figure 25(*b*) the curve fit used to measure u_τ is compared with various measurements in a PWJ from the literature. A typical measurement carried out as part of the current work is also shown. The agreement with the experimental data is good over the curve fit range ($4 \leqslant z^+ \leqslant 10$).

https://doi.org/10.1017/jfm.2019.559 Published online by Cambridge University Press

REFERENCES

ABRAHAMSSON, H., JOHANSSON, B. & LÖFDAHL, L. 1994 A turbulent plane two-dimensional wall-jet in a quiescent surrounding. *Eur. J. Mech. (*B*/Fluids)* **13**, 533–556.

ADRIAN, R. J. 2007 Hairpin vortex organization in wall turbulence. *Phys. Fluids* **19** (4), 041301.

ADRIAN, R. J., MEINHART, C. D. & TOMKINS, C. D. 2000 Vortex organization in the outer region of the turbulent boundary layer. *J. Fluid Mech.* **422**, 1–54.

AHLMAN, D., BRETHOUWER, G. & JOHANSSON, A. V. 2007 Direct numerical simulation of a plane turbulent wall-jet including scalar mixing. *Phys. Fluids* **19** (6), 065102.

DEL ÁLAMO, J. C. & JIMÉNEZ, J. 2006 Linear energy amplification in turbulent channels. *J. Fluid Mech.* **559**, 205–213.

BAARS, W. J., TALLURU, K. M., HUTCHINS, N. & MARUŠIĆ, I. 2015 Wavelet analysis of wall turbulence to study large-scale modulation of small scales. *Exp. Fluids* **56** (10), 188.

BAIDYA, R. 2016 Multi-component velocity measurements in turbulent boundary layers. PhD thesis, The University of Melbourne.

BAILEY, S. C. C. & SMITS, A. J. 2010 Experimental investigation of the structure of large- and very-large-scale motions in turbulent pipe flow. *J. Fluid Mech.* **651**, 339–356.

BALAKUMAR, B. J. & ADRIAN, R. J. 2007 Large- and very-large-scale motions in channel and boundary-layer flows. *Phil. Trans. R. Soc. Lond.* A **365** (1852), 665–681.

BANDYOPADHYAY, P. R. & HUSSAIN, A. K. M. F. 1984 The coupling between scales in shear flows. *Phys. Fluids* **27** (9), 2221–2228.

BANYASSADY, R. & PIOMELLI, U. 2014 Turbulent plane wall jets over smooth and rough surfaces. *J. Turbul.* **15** (3), 186–207.

BANYASSADY, R. & PIOMELLI, U. 2015 Interaction of inner and outer layers in plane and radial wall jets. *J. Turbul.* **16** (5), 460–483.

BRADSHAW, B. A. & GEE, M. T. 1960 Turbulent wall jets with and without an external stream. *NPL Bull.* **3252**, 51.

BROWAND, F. K. 1986 The structure of the turbulent mixing layer. *Physica* D **18** (1), 135–148.

BROWN, G. L. & THOMAS, A. S. W. 1977 Large structure in a turbulent boundary layer. *Phys. Fluids* **20** (10), S243–S252.

CHAUHAN, K. A., MONKEWITZ, P. A. & NAGIB, H. M. 2009 Criteria for assessing experiments in zero pressure gradient boundary layers. *Fluid Dyn. Res.* **41** (2), 021404.

CHRISTENSEN, K. T. 2001 Experimental investigation of acceleration and velocity fields in turbulent channel flow. PhD thesis, University of Illinois at Urbana-Champaign.

CHRISTENSEN, K. T. & ADRIAN, R. J. 2001 Statistical evidence of hairpin vortex packets in wall turbulence. *J. Fluid Mech.* **431**, 433–443.

CHUNG, D. & MCKEON, B. J. 2010 Large-eddy simulation of large-scale structures in long channel flow. *J. Fluid Mech.* **661**, 341–364.

DE GRAAFF, D. & EATON, J. K. 2000 Reynolds-number scaling of the flat-plate turbulent boundary layer. *J. Fluid Mech.* **422**, 319–346.

DEJOAN, A. & LESCHZINER, M. A. 2005 Large eddy simulation of a plane turbulent wall jet. *Phys. Fluids* **17** (2), 025102.

DEJOAN, A. & LESCHZINER, M. A. 2006 Separating the effects of wall blocking and near-wall shear in the interaction between the wall and the free shear layer in a wall jet. *Phys. Fluids* **18** (6), 065110.

DEJOAN, A. & LESCHZINER, M. A. 2007 On the near-wall structure in reverse-flow and post-reattachment recovery regions of separated flow and its equivalence to the structure in wall and free-surface jets. *J. Turbul.* **8**, N14.

DOGAN, E., HANSON, R. E. & GANAPATHISUBRAMANI, B. 2016 Interactions of large-scale free-stream turbulence with turbulent boundary layers. *J. Fluid Mech.* **802**, 79–107.

DUNN, M. 2010 An experimental study of a plane turbulent wall jet using particle image velocimetry. Master's thesis, University of Saskatchewan.

DUVVURI, S. & MCKEON, B. J. 2015 Triadic scale interactions in a turbulent boundary layer. *J. Fluid Mech.* **767**, R4.

https://doi.org/10.1017/jfm.2019.559 Published online by Cambridge University Press

ERIKSSON, J. G., KARLSSON, R. I. & PERSSON, J. 1998 An experimental study of a two-dimensional plane turbulent wall jet. *Exp. Fluids* **25** (1), 50–60.

GANAPATHISUBRAMANI, B., HUTCHINS, N., MONTY, J. P., CHUNG, D. & MARUŠIĆ, I. 2012 Amplitude and frequency modulation in wall turbulence. *J. Fluid Mech.* **712**, 61–91.

GEORGE, W. K., ABRAHAMSSON, H., ERIKSSON, J., KARLSSON, R. I., LÖFDAHL, L. & WOSNIK, M. 2000 A similarity theory for the turbulent plane wall jet without external stream. *J. Fluid Mech.* **425**, 367–411.

GUALA, M., HOMMEMA, S. E. & ADRIAN, R. J. 2006 Large-scale and very-large-scale motions in turbulent pipe flow. *J. Fluid Mech.* **554**, 521–542.

GUALA, M., METZGER, M. & MCKEON, B. J. 2011 Interactions within the turbulent boundary layer at high Reynolds number. *J. Fluid Mech.* **666**, 573–604.

HAMMOND, G. P. 1982 Complete velocity profile and 'optimum' skin friction formulas for the plane wall-jet. *Trans. ASME J. Fluids Engng* **104**, 59–65.

HARUN, Z., MONTY, J. P., MATHIS, R. & MARUŠIĆ, I. 2013 Pressure gradient effects on the large-scale structure of turbulent boundary layers. *J. Fluid Mech.* **715**, 477–498.

HEARST, R. J., DOGAN, E. & GANAPATHISUBRAMANI, B. 2018 Robust features of a turbulent boundary layer subjected to high-intensity free-stream turbulence. *J. Fluid Mech.* **851**, 416–435.

HUTCHINS, N. & CHOI, K.-S. 2002 Robust features of a turbulent boundary layer subjected to high-intensity free-stream turbulence. *Prog. Aerosp. Sci.* **38** (4–5), 421–446.

HUTCHINS, N. & MARUŠIĆ, I. 2007*a* Evidence of very long meandering features in the logarithmic region of turbulent boundary layers. *J. Fluid Mech.* **579**, 1–28.

HUTCHINS, N. & MARUŠIĆ, I. 2007*b* Large-scale influences in near-wall turbulence. *Phil. Trans. R. Soc. Lond.* A **365** (1852), 647–664.

HUTCHINS, N., MONTY, J. P., GANAPATHISUBRAMANI, B., NG, H. C. H. & MARUŠIĆ, I. 2011 Three-dimensional conditional structure of a high-Reynolds-number turbulent boundary layer. *J. Fluid Mech.* **673**, 255–285.

HUTCHINS, N., NICKELS, T. B., MARUŠIĆ, I. & CHONG, M. S. 2009 Hot-wire spatial resolution issues in wall-bounded turbulence. *J. Fluid Mech.* **635**, 103–136.

IRWIN, H. P. A. H. 1973 Measurements in a self-preserving plane wall jet in a positive pressure gradient. *J. Fluid Mech.* **61** (1), 33–63.

JACOBI, I. & MCKEON, B. J. 2013 Phase relationships between large and small scales in the turbulent boundary layer. *Exp. Fluids* **54** (3), 1481.

JIMÉNEZ, J. 2012 Cascades in wall-bounded turbulence. *Annu. Rev. Fluid Mech.* **44**, 27–45.

KARLSSON, R. I., ERIKSSON, J. & PERSSON, J. 1993*a* An experimental study of a two-dimensional plane turbulent wall jet. *Tech. Rep.* Report VU-S 93:B36. Vattenfall Utveckling AB, lvkarleby, Sweden.

KARLSSON, R. I., ERIKSSON, J. & PERSSON, J. 1993*b* LDV measurements in a plane wall jet in a large enclosure. In *Laser Techniques and Applications in Fluid Mechanics: Proceedings of the 6th International Symposium, Lisbon, Portugal, 20–23, July 1992*.

KATZ, Y., HOREV, E. & WYGNANSKI, I. 1992 The forced turbulent wall jet. *J. Fluid Mech.* **242**, 577–609.

KLINE, S. J., REYNOLDS, W. C., SCHRAUB, F. A. & RUNSTADLER, P. W. 1967 The structure of turbulent boundary layers. *J. Fluid Mech.* **30** (4), 741–773.

KULANDAIVELU, V. 2011 Evolution and structure of zero pressure gradient turbulent boundary layer. PhD thesis, University of Melbourne.

LAUNDER, B. E. & RODI, W. 1981 The turbulent wall jet. *Prog. Aerosp. Sci.* **19**, 81–128.

LAUNDER, B. E. & RODI, W. 1983 The turbulent wall jet measurements and modeling. *Annu. Rev. Fluid Mech.* **15** (1), 429–459.

LEE, J. H. & SUNG, H. J. 2013 Comparison of very-large-scale motions of turbulent pipe and boundary layer simulations. *Phys. Fluids* **25** (4), 045103.

LEE, M. & MOSER, R. D. 2015 Direct numerical simulation of turbulent channel flow up to $Re_\tau \approx$ 5200. *J. Fluid Mech.* **774**, 395–415.

LOUCKS, R. B. & WALLACE, J. M. 2012 Velocity and velocity gradient based properties of a turbulent plane mixing layer. *J. Fluid Mech.* **699**, 280–319.

https://doi.org/10.1017/jfm.2019.559 Published online by Cambridge University Press

MARUŠIĆ, I. & HEUER, W. D. C. 2007 Reynolds number invariance of the structure inclination angle in wall turbulence. *Phys. Rev. Lett.* **99** (11), 114504.

MARUŠIĆ, I., MCKEON, B. J., MONKEWITZ, P. A., NAGIB, H. M., SMITS, A. J. & SREENIVASAN, K. R. 2010 Wall-bounded turbulent flows at high Reynolds numbers: recent advances and key issues. *Phys. Fluids* **22**, 065103.

MATHIS, R., HUTCHINS, N. & MARUŠIĆ, I. 2009*a* Large-scale amplitude modulation of the small-scale structures in turbulent boundary layers. *J. Fluid Mech.* **628**, 311–337.

MATHIS, R., HUTCHINS, N. & MARUŠIĆ, I. 2011*a* A predictive inner–outer model for streamwise turbulence statistics in wall-bounded flows. *J. Fluid Mech.* **681**, 537–566.

MATHIS, R., MARUŠIĆ, I., HUTCHINS, N. & SREENIVASAN, K. R. 2011*b* The relationship between the velocity skewness and the amplitude modulation of the small scale by the large scale in turbulent boundary layers. *Phys. Fluids* **23** (12), 121702.

MATHIS, R., MONTY, J. P., HUTCHINS, N. & MARUŠIĆ, I. 2009*b* Comparison of large-scale amplitude modulation in turbulent boundary layers, pipes, and channel flows. *Phys. Fluids* **21** (11), 111703.

MONTY, J. P., HUTCHINS, N., NG, H. C. H., MARUŠIĆ, I. & CHONG, M. S. 2009 A comparison of turbulent pipe, channel and boundary layer flows. *J. Fluid Mech.* **632**, 431–442.

NAQAVI, I. Z., TYACKE, J. C. & TUCKER, P. G. 2018 Direct numerical simulation of a wall jet: flow physics. *J. Fluid Mech.* **852**, 507–542.

NARASIMHA, R., NARAYAN, K. Y. & PARTHASARATHY, S. P. 1973 Parametric analysis of turbulent wall jets in still air. *Aeronaut. J.* **77**, 335–359.

NUGROHO, B., HUTCHINS, N. & MONTY, J. P. 2013 Large-scale spanwise periodicity in a turbulent boundary layer induced by highly ordered and directional surface roughness. *Intl J. Heat Fluid Flow* **41**, 90–102.

PATHIKONDA, G. & CHRISTENSEN, K. T. 2017 Inner-outer interactions in a turbulent boundary layer overlying complex roughness. *Phys. Rev. Fluids* **2**, 044603.

PEROT, B. & MOIN, P. 1995 Shear-free turbulent boundary layers. Part 1. Physical insights into near-wall turbulence. *J. Fluid Mech.* **295**, 199–227.

POPE, S. B. 2001 *Turbulent Flows*. IOP Publishing.

RAULEDER, J. & LEISHMAN, J. G. 2014 Flow environment and organized turbulence structures near a plane below a rotor. *AIAA J.* **52** (1), 146–161.

ROGERS, M. M. & MOSER, R. D. 1994 Direct simulation of a self-similar turbulent mixing layer. *Phys. Fluids* **6** (2), 903–923.

ROSTAMY, N., BERGSTROM, D. J., SUMNER, D. & BUGG, J. D. 2011*a* The effect of surface roughness on the turbulence structure of a plane wall jet. *Phys. Fluids* **23** (8), 2043–2050.

ROSTAMY, N., BERGSTROM, D. J., SUMNER, D. & BUGG, J. D. 2011*b* An experimental study of a turbulent wall jet on smooth and transitionally rough surfaces. *J. Fluids Engng* **133** (11), 111207.

SAMIE, M., MARUŠIĆ, I., HUTCHINS, N., FU, M. K., FAN, Y., HULTMARK, M. & SMITS, A. J. 2018 Fully resolved measurements of turbulent boundary layer flows up to $Re_\tau = 20\,000$. *J. Fluid Mech.* **851**, 391–415.

SCHLATTER, P. & ORLU, R. 2010 Quantifying the interaction between large and small scales in wall-bounded turbulent flows: a note of caution. *Phys. Fluids* **22** (5), 1–4.

SCHNEIDER, M. E. & GOLDSTEIN, R. J. 1994 Laser Doppler measurement of turbulence parameters in a two-dimensional plane wall jet. *Phys. Fluids* **6** (9), 3116–3129.

SCHOBER, M. & FERNHOLZ, H.-H. 2000 Turbulence control in wall jets. *Eur. J. Mech. (B/Fluids)* **19** (4), 503–528.

SHARP, N. S., NEUSCAMMAN, S. & WARHAFT, Z. 2009 Effects of large-scale free stream turbulence on a turbulent boundary layer. *Phys. Fluids* **21** (9), 095105.

SILLERO, J. A., JIMÉNEZ, J. & MOSER, R. D. 2013 One-point statistics for turbulent wall-bounded flows at Reynolds numbers up to $\delta^+ \approx 2000$. *Phys. Fluids* **25** (10), 105102.

SILLERO, J. A., JIMÉNEZ, J. & MOSER, R. D. 2014 Two-point statistics for turbulent boundary layers and channels at Reynolds numbers up to $\delta^+ \approx 2000$. *Phys. Fluids* **26** (10), 105109.

https://doi.org/10.1017/jfm.2019.559 Published online by Cambridge University Press

SMITH, B. 2008 Wall jet boundary layer flows over smooth and rough surfaces. PhD thesis, Virginia Polytechnic Institute and State University, Blacksburg, VA.

SMITS, A. J., MCKEON, B. J. & MARUŠIĆ, I. 2011 High-Reynolds number wall turbulence. *Annu. Rev. Fluid Mech.* **43**, 353–375.

TACHIE, M., BALACHANDAR, R. & BERGSTROM, D. 2002 Scaling the inner region of turbulent plane wall jets. *Exp. Fluids* **33** (2), 351–354.

TACHIE, M. F., BALACHANDAR, R. & BERGSTROM, D. J. 2004 Roughness effects on turbulent plane wall jets in an open channel. *Exp. Fluids* **37** (2), 281–292.

TALLURU, K. M., BAIDYA, R., HUTCHINS, N. & MARUŠIĆ, I. 2014 Amplitude modulation of all three velocity components in turbulent boundary layers. *J. Fluid Mech.* **746**, R1.

TOWNSEND, A. A. 1976 *The Structure of Turbulent Shear Flow*. Cambridge University Press.

TUTKUN, M., GEORGE, W. K., DELVILLE, J., STANISLAS, M., JOHANSSON, P. B. V., FOUCAUT, J.-M. & COUDERT, S. 2009 Two-point correlations in high Reynolds number flat plate turbulent boundary layers. *J. Turbul.* **10**, N21.

VENÅS, B., ABRAHAMSSON, H., KROGSTAD, P. Å & LÖFDAHL, L. 1999 Pulsed hot-wire measurements in two- and three-dimensional wall jets. *Exp. Fluids* **27** (3), 210–218.

VOLINO, R. J., SCHULTZ, M. P. & FLACK, K. A. 2007 Turbulence structure in rough-and smooth-wall boundary layers. *J. Fluid Mech.* **592**, 263–293.

WU, Y. & CHRISTENSEN, K. T. 2010 Spatial structure of a turbulent boundary layer with irregular surface roughness. *J. Fluid Mech.* **655**, 380–418.

WYGNANSKI, I., KATZ, Y. & HOREV, E. 1992 On the applicability of various scaling laws to the turbulent wall jet. *J. Fluid Mech.* **234**, 669–690.

ZHOU, M. D., HEINE, C. & WYGNANSKI, I. 1993 The forced turbulent wall jet in an external stream. In *3rd Shear Flow Conference, Orlando, FL. AIAA Paper* 93-3250. AIAA.

ZHOU, M. D., HEINE, C. & WYGNANSKI, I. 1996 The effects of excitation on the coherent and random motion in a plane wall jet. *J. Fluid Mech.* **310**, 1–37.

https://doi.org/10.1017/jfm.2019.559 Published online by Cambridge University Press